First Principles Studies of MCO_3 (M: Ca, Mn, Fe, Co, Ni) Precursor Materials for Li-ion Batteries

by

MOGAHABO TEBOGO MORUKULADI

RESEARCH DISSERTATION

Submitted in fulfilment of the requirement for the degree of

MASTER OF SCIENCE

In

Physics

In the

FACULTY OF SCIENCE & AGRICULTURE

(School of Physical & Mineral Sciences)

at the

UNIVERISTY OF LIMPOPO (Turf loop Campus)

SUPERVISOR: Prof P.E Ngoepe

Co- SUPERVISORS: Dr N.L Lethole

: Dr M.C Masedi

: Dr N.N Ngoepe

2020

Declaration

I declare that the dissertation hereby submitted to the University of Limpopo (Turf-loop Campus) for the degree of Master of Science has not previously been submitted by me or any other person for a degree at this or any other institution, that it is my own work both in design and execution, and that all materials contained herein has been duly acknowledged.

Ms MT Morukuladi

Signature

Dedications

This work is dedicated to my wonderful mom Molatelo Rebecca Morukuladi and my sisters Maria, Emily, Girly and Charlotte Morukuladi, thank you for encouraging me to further my studies, your support strengthened me daily and I really appreciate it. If it were not by your daily advices, I wound not have been here. This work is also dedicated to my son Ofentse and also my late father Matee Johannes Morukuladi, may your soul continue to rest in peace papa.

Acknowledgement

First and foremost, I would like to thank God for being with me throughout this work. I also want to express my sincere gratitude and appreciation to my supervisor and core-supervisors Prof P.E Ngoepe, Dr N.L Lethole, Dr N.N Ngoepe and Dr M.C Masedi for leading me into the scientific research of materials science, their great patience, professional guidance and continuous support during my studies. I also want to thank all my colleagues at the Materials Modelling Centre for helpful discussions and countless friendship. Last but not least, I would like to express my deepest gratitude to my wonderful family, they stood by me in all the situations I came through in my studies and supported each and every decision I took and never lost hope, for that I thank and love you so much.

The financial support from National Research Foundation is also highly appreciated.

Abstract

The need for improved, reliable and efficient energy storage devices such as lithium-ion rechargeable batteries have increased, in particular the cathode materials for Li-ion batteries. The currently used cathode material lithium cobalt oxide (LCO) have been reported to be toxic, expensive and scarcity of cobalt. However, Nickel Manganese Cobalt (NMC) have been reported as alternate cathode materials for lithium ion batteries due to their availability, affordability and non-toxic nature. Moreover, Lithium and manganese-rich composites $Li_{1+x}M_{1-x}O_2$ have gained lots of attention as future cathode materials for Li-ion batteries due to their high capacity (>250mAh/g) and improved structural stability. The electrochemical performances of these compounds depends mainly on the physical properties of the precursor material which are synthesised via calcination. Precursor materials serve as source of lithium in lithium and manganese rich composites. Generally, precursor materials are a mixture of two or more substances that occur in a chemical reaction yielding other substances at the completion of a chemical reaction.

In this work we initially perform preliminary first-principles density functional theory (DFT) studies to investigate the structural, thermodynamic, electronic and mechanical properties for transition metal carbonate precursor materials using the Vienna *ab*-initio simulation package (VASP) code. In particular, we calculate the cell parameters, heats of formation, density of states, band structures, elastic constants and phonon dispersion curves to mimic stability trend for MCO_3. Moreover, cluster expansion methods were employed to determine the phase stability of $Ni_{1-x}Mn_xCO_3$, $Co_{1-x}Ni_xCO_3$, and $Co_{1-x}Mn_xCO_3$ structures using the Universal Cluster Expansion (UNCLE) code. The structural lattice parameters were calculated to 95% agreement with the experimental data, ensuring robustness of the approach employed. The thermodynamic heats of formation were predicted to increase with the atomic mass of the

transition metal except for $CoCO_3$ and $NiCO_3$, suggesting that $CaCO_3$ is the most stable carbonate while $CoCO_3$ is least stable. From the calculated elastic properties, we noted that transition metal carbonates in $CaCO_3$, $MnCO_3$, $CoCO_3$ and $NiCO_3$ satisfied the necessary stability criterion for trigonal crystal system, suggesting mechanical stability. On the other hand, $FeCO_3$ was predicted to be unstable since the stability criterion $(C_{44} + C_{12})C_{33} - 2C_{13}^2 > 0$ and $(C_{11} + C_{12})C_{44} - 2C_{14}^2 > 0$ were not satisfied. The calculated phonon dispersion curves showed positive vibrations in the Brillouin zone indicating vibrational stability for $CaCO_3$, $MnCO_3$, $NiCO_3$ and $CoCO_3$ while on the other hand $FeCO_3$ displayed the negative vibrations along the high Brillouin zone suggesting vibrational instability. The analysis of electronic structures showed that $CaCO_3$ and $MnCO_3$ are insulators due to the presence of relatively wide band gaps. On the other hand, $CoCO_3$ and $NiCO_3$ are semiconductors while $FeCO_3$ showed metallic behaviour. Furthermore, the binary phase diagram from cluster expansion calculations generated new mixed $Ni_{1-x}Mn_xCO_3$ phases with the most stable phase favouring the Mn-rich side while $Co_{1-x}Ni_xCO_3$ and $Co_{1-x}Mn_xCO_3$ are favourable at equiatomic (50:50) concentration.

Table of Contents

List of Figures

List of Tables

List of Abbreviations

BCC	**Base Centred Cubic**
$CaCO_3$	**Calcium Carbonate**
CE	**Cluster Expansion**
$CoCO_3$	**Cobalt Carbonate**
CVS	**Coefficient of Variations**
DFT	**Density Functional Theory**
DOS	**Density of States**
FCC	**Face Centred Cubic**
$FeCO_3$	**Iron Carbonate**
GGA	**Generalized Gradient Approximation**
LA	**Longitudinal Acoustic**
LCO	**Lithium Cobalt Oxide**
LDA	**Local Density Approximation**
LIBS	**Lithium Ion Batteries**
LO	**Longitudinal Optical**
MD	**Molecular Dynamics**
$MnCO_3$	**Manganese Carbonate**
$NiCO_3$	**Nickel Carbonate**
NMC	**Nickel Manganese Cobalt**
PAW	**Project Augmented Wave**
PW	**Plane-Waves**
SIESTA	**Spanish Initiative for Electronic Simulations with Thousand Atoms**
TA	**Transverse Acoustic**
TO	**Transverse Optical**
U	**Hubbard Parameter**
UNCLE	**Universal Cluster Expansion**

VASP **Vienna ab initio Simulation Package**

CHAPTER 1

1.1. Rationale

Different types of batteries have been developed and commercialised over the past few decades. For instance, nickel-cadmium batteries, nickel-metal hydride batteries, and lithium-ion batteries are some of the different types of popular batteries which are now commercially available [1]. Of all the different types of batteries available and currently developed, lithium-ion batteries (LIBs) have gained a significant segmentation in the market and are the most promising and the fastest growing battery technology [2]**.** They offer very high energy densities, have low self-discharge and can operate at higher voltage of 3.7V compared to other battery candidates, which offer only up to 1.2V [3]. Since Li-ion batteries are the first choice source of portable electrochemical energy storage, improving performance and reduction of their high costs can greatly expand their applications and enable new technologies which depend on energy storage. However, the performance of any Li-ion battery greatly depends on the physical and chemical properties of the cathode material, which serves as a host for Li ions.

Cathode materials are crucial components in Li-ion batteries and have aroused great interests due to the different chemistries of cathode materials such as nickel cobalt aluminium (NCA), spinel lithium manganese oxide (LMO), lithium iron phosphate (LFP) and lithium cobalt oxide ion (LCO) [4]. Amongst these cathode materials, $LiCoO_2$ (LCO) has been the most widely used and commercialised cathode material [5], however this material was found to be toxic, very expensive and exhibiting low theoretical capacity of 140 mAh/g when $LiCoO_2$ is cycled between 3V and 4.2V, hence hindering the widespread application in lithium-ion batteries [6]. Different chemistries of cathode materials such as LCO, LFP and LMO were also reported to have drawbacks such as being toxic, expensive and scarce [7]. As a result of drawbacks displayed by the well-studied cathode materials, there has been an extensive quest to find

cathode materials with high volumetric density and high specific reversible discharge capacity for application in Li-ion batteries.

NCM (nickel, cobalt, manganese) composites have recently attracted a lot of interest due to their low cost and less toxicity than widely commercialised LCO. Amongst these, composite lithium and manganese rich compounds have even become more attractive cathode materials due to their high capacity and also improved structural stability [8, 9]. However the electrochemical performance of these composites materials strongly depends upon the physical properties of the precursor materials that serve as source for lithium [10]. Precursor materials are a mixture of two or more substances that occurs in a chemical reaction yielding other substances. Currently, Li-ion battery materials largely use the hydroxide co-precipitation to produce the transition metal hydroxide precursors [11]. The problem with hydroxide co-precipitation is that the oxidation of the cation is possible, which means cations may oxidise to higher than the 2^+ valency, specifically manganese oxidation leading to deviation from the desired stoichiometry. Consequently, carbonate co-precipitation has emerged as a promising candidate to produce the transition metal carbonate precursor materials, with the advantage being that in carbonate matrix, the oxidation state is kept as 2^+ throughout [12, 13]. The carbonate co-precipitation method results in a homogeneous and phase-pure precursor in which the oxidation state of the cation is kept as 2^+ for all the transition metals, and it can be used for the synthesis of a more homogeneous and pure lithium- and manganese-rich material with high electrochemical performance. Co-precipitation is a popular approach to synthesise precursors for transition metal oxide cathode materials used in lithium-ion batteries. The morphology of precursor particles can be retained after the insertion of transition metal to obtain final active materials of tuneable size and shape. Hence, in this work we investigate the structural, energetic, electronic, elastic and vibrational properties of the transition metal carbonate (MCO_3) precursor materials by mimicking their stability trends at ambient conditions. In

particular, we calculate the cell parameters, heats of formation, band structures, densities of states, elastic constants and phonon dispersion curves. Furthermore, we also investigate the phase stability of MCO_3 precursors considered by generating their phase diagrams. Hence, we hope to produce more improved, desirable and non-toxic transition metal carbonate precursor cathode materials for Li-ion batteries for future generation.

1.2. Literature Review

Several transition metal carbonates (MCO_3) have been reported to exist in nature, particularly $CaCO_3$, $MnCO_3$, $MgCO_3$ and $FeCO_3$. Carbonates are amongst the most common sediments on earth crust, with calcium and magnesium carbonates storing the majority of the total carbon [14]. Calcium carbonates which are in amorphous state and soluble in acid water exist as bio-minerals composed of calcium and carbonate ions. These carbonates are also referred to as Amorphous Calcium Carbonates (ACC) [15].

Calcium carbonate crystallises in three types of structural polymorphs namely; calcite, aragonite and vaterite [16]. Calcite has a rhombohedral crystal structure with lattice parameters $a = b = -4.990\text{Å}$ $c = -17.061\text{Å}$ and it is the most stable form of $CaCO_3$ in the environment. It is stable at atmospheric pressure and temperature and only decomposes at 973 K. The Ca^{2+} and CO_3^{2-} ions in calcite are held together through the ionic bonding and it is easy to cleave the crystal, as an external force can cause a plane of atoms to shift into a position where ions with the same charge are next to each other, causing repulsive and cleavage. Aragonite has an orthorhombic crystal structure with space group *PmCn* with lattice $a = 4.960\text{Å},\ b = 7.964\text{Å},\ c = 5.738\text{Å}\ and\ \alpha = \beta = \gamma = 90°$.

The vaterite polymorph has a different crystal structure from those of calcite and aragonite in terms of symmetry, orientation of carbonate ion and coordination environment of calcium ions. There is an agreement that Ca atoms are in eight-fold coordination with oxygen atoms. Calcium

atoms have six-fold coordination in calcite and nine-fold coordination in aragonite [17]. Deer *et al* reported that vaterite has a hexagonal crystal structure with space group P63 and $a = b = 4.13\text{Å}, c = 8.48\text{Å}\ and\ \alpha = \beta = 90°, \gamma = 120°$ [18].

$MnCO_3$ with the chemical name rhodochrosite is a mineral which crystallises with a hexagonal calcite-type structure. Layers of manganese cations alternate with parallel $(CO_3)^{2-}$ groups with manganese featuring on the octahedral coordination. $FeCO_3$ with the chemical name siderite forms in environments where O_2 is scarce. $FeCO_3$ crystallises in a rhombohedral calcite-type structure of R3cH symmetry formed by corner-shared trigonal planar. $NiCO_3$ and $CoCO_3$ used in this study have the rhombohedral crystal structure with space group R3cH. However, $CaCO_3$ and $FeCO_3$ are not routinely used to make precursors, hence in this study we compare them with known precursors namely $NiCO_3$, $MnCO_3$ and $CoCO_3$.

1.3. Intensions of the study

Lithium-ion batteries are widely and increasingly used in many portable electronic devices and high-power systems in the modern society. Currently, it is significant to develop excellent cathode materials to meet stringent standards for batteries. $LiCoO_2$ is the most highly used cathode material in portable electronic devices. However, due to cobalt being scarce, toxic and expensive, it has led $LiCoO_2$ to be an imperfect cathode material. As such, the layered $Li_{1+x}(NMC)_{1-x}O_2$ are considered as alternative cathode materials due to their high capacity (>200mAh/g), higher voltage, great structural stability, affordability and improved safety. Hence, in this study we investigate the transition metal carbonate (MCO_3) as precursors for lithium ion batteries using first principles density functional theory (DFT). We employ plane wave pseudopotential techniques as embodied in the VASP code for equilibrium ground state properties and PHONON code for determining their vibrational properties. The main purpose of this work is to attain the fundamental understanding on stabilities of transition metal

carbonates at 0K. Five properties will be calculated to determine stability; namely structural, energetic, electronic, mechanical and vibrational properties. We particularly calculate the equilibrium cell parameters, heats of formations, band structures, density of states, elastic constants and phonon dispersion curves. Five transition metal carbonates considered in this study are namely $CaCO_3$, $MnCO_3$, $FeCO_3$, $CoCO_3$ and $NiCO_3$.

1.4. Outline of the study

Chapter 1 contains the general background of MCO_3 (Ca, Mn, Fe, CO, Ni) structures for lithium ion batteries. The structural aspects of MCO_3 structures are discussed in this chapter. Also, the rationale and intensions of the study are outlined in this chapter.

Chapter 2 discusses theoretical aspects and methodologies used throughout this work, in particular the computational techniques, such as energy minimisation and electronic structure methods.

Chapter 3 discusses the *ab* initio results for MCO_3 structures and compare them with the available experimental data.

Chapter 4 contains cluster expansion and Monte Carlo background. The methodology used and the results on phase stability for cluster expansion are also outlined in this chapter. Finally, a short summary of the main results presented in this thesis and several citations are also listed in this chapter.

CHAPTER 2
Theoretical techniques

2.1. Introduction

In this chapter we intend to report on the theoretical background and computational methods employed in this study. We will be using computer simulation techniques which offers an alternative way of investigating properties of materials (using computers), whereby the simulator builds a model of a real system and explores its behaviour. The mathematical model is physically based with the exploration being done on a computer. In many ways these simulation studies share the same mentality as experimental investigations. However, in a simulation there is absolute control and access to detail and given enough computer power, exact answers for the model. The commonly known computational technique is based on *ab initio* method. An *Ab initio* is a group of methods in which properties of materials i.e. the values of the fundamental constants and the atomic numbers of the atoms present can be calculated using Schrödinger equation. These methods include density functional theory (DFT), Hartree-Fock (HF) methods and post-Hartree-Fock (PHF) methods. In the current study, we will only focus on the density functional theory for predicting the ground-state energies of many-body system. We discuss the implementation of the plane-wave pseudopotentials, VASP and PHONON codes which are embedded within MedeA software.

2.2. Density functional theory

Density functional theory (DFT) is a quantum mechanical theory used in physics and chemistry to study the electronic structure and ground state properties of many body systems. The theory was based on formulae by Hohenberg and Kohn [19] Sham in the 1960's using two theorems to provide the foundation of accurate calculations. The first theorem states that for any system of interacting particles in an external potential $V(r)$, the external potential is uniquely

determined by the ground state density [20]. This theorem provides essential foundation for reducing a many-body system by the use of functional of the electron density.

$$E = E[\rho] \tag{2-1}$$

Where E is the total energy and ρ is the electron density. In DFT, the total electron density is decomposed into one-electron density which is constructed from one-electron wave functions. The idea of using the electron density as the fundamental entity of a quantum mechanical theory of matter originates in the early days of quantum mechanics in the 1920's, especially from the work of Thomas and Fermi [21]. However, in the subsequent decades, it was rather the Hartree-Fock approach [22], which was developed and applied to small molecular systems. Calculations on realistic solid state systems were then out of reach. In 1951, Slater [23] used ideas from the electron gas with the intention to simplify Hartree-Fock theory to a point where electronic structure calculations on solids became feasible. Slater's work, which led to the so-called $X\alpha$ method, has contributed tremendously to the development of electronic structure calculations. In solid-state systems, the electron density is a scalar function defined at each point r in real space,

$$\rho = \rho(r) \tag{2-2}$$

The electron density and the total energy depend on the type and arrangements of the atomic nuclei. Therefore, one can write

$$E = E\left[\rho(r), \{R_\alpha\}\right] \tag{2-3}$$

where the set $\{R_\alpha\}$ denotes the positions of all atoms in the system under consideration. Equation (2-3) is the key to an atomic-scale understanding of electronic, structural and dynamic properties of matter. If one has a way of evaluating expression (2-3), one can for example, predict the equilibrium structure of solid and predict the reconstruction of surfaces and the

equilibrium geometry of molecules adsorbed on surfaces. Furthermore, the derivative of the total energy (2-3) with respect to the nuclear position of an atom gives the force acting on that atom. This enables the efficient search for stable structures and more importantly for the study of dynamical processes such as diffusion or the reaction of molecules on surfaces. Most of the considerations discussed here are based on the Born-Oppenheimer approximation [24] in which it is assumed that the motions of the electrons are infinitely faster than those of the nuclei. In practice this means that the electronic structure is calculated for a fixed atomic arrangement and the atoms are then moved according to classical mechanics. This is a fairly good approximation for heavy atoms like tungsten (W), but may cause errors for light atoms such as hydrogen (H) or lithium (Li).

In density functional theory, the total energy is decomposed into three contributions namely; a kinetic energy (T_0), Coulomb energy due to classical electrostatic interactions among all charged particles in the system (U) and a term called exchange-correlation energy (E_{XC})that captures all many-body interactions.

$$E = T_0 + U + E_{XC}. \qquad (2\text{-}4)$$

Where T_0 is the kinetic energy, U is the Coulomb energy and E_{XC} is the exchange correlation energy. It is purely classical and contains the electrostatic energy arising from the Coulomb attraction between electrons and nuclei, the repulsion between all electronic charges and the repulsion between nuclei. It can be written as follows;

$$U = U_{en} + U_{ee} + U_{nn} \quad , \qquad (2\text{-}5)$$

with

$$U_{en} = -e^2 \sum_{\alpha} Z_{\alpha} \int \frac{\rho(r)}{|r - R_{\alpha}|} dr \quad , \qquad (2\text{-}6)$$

$$U_{ee} = e^2 \iint \frac{\rho(r)\rho(r')}{|r - r'|} dr dr' \quad , \tag{2-7}$$

$$U_{nn} = e^2 \sum_{\alpha\alpha'} \frac{Z_\alpha Z_{\alpha'}}{|R_\alpha - R_{\alpha'}|} \quad , \tag{2-8}$$

where e is the elementary charge of a proton and $Z'_\alpha$is the atomic number of atom α. The summations extend over all atoms and the integrations over all space. Once the electron density, atomic numbers and positions of all atoms are known, expression (2-6) to (2-8) can be evaluated by using the techniques of classical electrostatics.

In density functional theory, the "real" electrons of a system are replaced by "effective" electrons with the same charge, mass and density distribution. However, effective electrons move as independent particles in an effective potential, whereas the motion of a "real" electron is correlated with those of all other electrons. T_0 is referred to as the sum of kinetic energies of all effective electrons moving as independent particles. Often, one does not explicitly make this distinction between real and effective electrons.

If each effective electron is described by a single particle wave function, Ψ_i then the kinetic energy of all effective electron in the system is given by the following equation.

$$T_0 = \sum n_i \int \psi_i^*(r) \left[-\frac{\hbar^2}{2m} \nabla^2 \right] \psi_i(r) dr \tag{2-9}$$

Expression (2-9) is the sum of the expectation values of one-particle kinetic energies were n_i denotes the number of electrons in state i, Ψ_i is a single particle wave-function and [$\frac{-\hbar^2}{2m} \nabla^2$] is the time dependent Schrödinger equation. By construction, the dynamical correlations between the electrons are excluded from T_0.

The third term of Eq. (2-4) which is called the exchange-correlation energy, E_{xc} includes all remaining complicated electronic contributions to the total energy. The Hohenberg-Kohn-Sham theorem [25], which is a central part of density functional theory, states that the total energy is at its minimum value for the ground state density and that the total energy is stationary with respect to first-order variations in the density as shown in equation 2-10.

$$\frac{\partial E[\rho]}{\partial \rho}\Big|_{\rho=\rho_0} = 0 \tag{2-10}$$

In conjunction with the kinetic energy, we have introduced one-particle wave-function $\Psi_i(r)$, which generate the electron density.

$$\rho(r) = \sum_i n_i |\psi_i(r)|^2 \tag{2-11}$$

where n_i denotes the occupation number of the eigenstate i, which is represented by the one-particle wave function Ψ_i. By construction, $\rho(r)$ in Eq. (2-11) is the exact many-electron density.

The goal of the next step is the derivation of equations that can be used for practical density functional calculations. The variational condition (2-10) can be used to derive the conditions for the one-particle wave-functions that lead to the ground state density. To this end, one substitutes Eq. (2-11) in expression (2-10) and varies the total energy with respect to each wave function. This procedure leads to the following equations:

$$[\tfrac{\hbar^2}{2m}\triangle^2 + V_{eff}(r)]\varphi_i(r) = \varepsilon_i\varphi_i(r) \; where \; V_{eff}(r) = V_c(r) + \mu_{xc}[\rho(r)] \tag{2-12}$$

Equations (2-12) are called the Kohn-Sham [26] equations. The electron density, which corresponds to these wave-functions, is the ground state density which minimizes the total energy. As a consequence of the partitioning of the total energy (2-4), the Hamiltonian operator

in the Kohn-Sham equations (2-12) contains three terms, one for the kinetic energy, the second for the Coulomb potential and the third for the exchange-correlation potential. The kinetic energy term is the standard second-order differential operator of one-particle Schrödinger equations and its construction does not require specific knowledge of a system. In contrast, the Coulomb potential operator, $V_c(r)$ and the exchange-correlation potential operator, depend on the specific electron distribution in the system under consideration. The Coulomb or electrostatic potential $V_c(r)$ at point r is generated from the electric charges of all nuclei and electrons in the system. It can be evaluated directly in a real space using equation 2-13 as follows;

$$V_C(r) = -e^2 \sum_{\alpha} \frac{Z_\alpha}{|r - R_\alpha|} + e^2 \int \frac{\rho(r')}{|r - r'|} dr' \tag{2-13}$$

In condensed systems it is more convenient to use Poisson's equation shown in 2-14

$$\nabla^2 V_C(r) = -4\pi e^2 q(r) \tag{2-14}$$

to calculate the electrostatic potential. Here, $q(r)$ denotes both the electronic charge distribution $\rho(r)$ and the positive point charges of the nuclei at positions R_α. The exchange-correlation potential is related to the exchange-correlation energy by equation 2-15 below.

$$\mu_{xc}(r) = \frac{\partial E_{xc}[\rho(r)]}{\partial \rho(r)} \tag{2-15}$$

Equation (2-15) is formally exact in the sense that it does not contain any approximations to the complete many-body interactions. Therefore, from the above discussions, the Kohn-Sham total energy functional can be expressed as;

$$E = \frac{1}{2}\sum_{occ}\varepsilon_i + U_{nn} - \frac{e^2}{2}\iint\frac{\rho(r)\rho(r')}{|r-r'|}drdr' + E_{xc}[\rho(r)] - \int\rho(r)\mu_{xc}dr \quad (2\text{-}16)$$

In practice however, the exchange-correlation energy (and thus the exchange-correlation potential) is not known and one has to make approximations which will be discussed in the next section.

2.3. Approximation methods

2.3.1. Local density approximation

Local density approximation (LDA) is a set of approximations to the E_{xc} functional in DFT that is determined by the electronic density at each point in space. LDA demonstrates that E_{xc} is similar to that for a locally uniform electron gas with similar density in regions where there is slow variation in charge density [27]. Several different schemes have been developed for obtaining approximate forms for the functional exchange-correlation energy. The simplest accurate approximation, for non-magnetic systems is to assume that the exchange-correlation energy is dependent only on the local electron density $d(r)$ around each volume element. Local density approximation (LDA) gives the correct sum rule for the exchange correlation hole [28].In the local density approximation the exchange correlation energy is given by equation 2-17;

$$E_{xc}[\rho] \approx \int\rho(r)\varepsilon_{xc}^{0}[\rho(r)]dr \quad (2\text{-}17)$$

Where $\rho(r)$ is the electron density while ε_{xc}^{0} denotes the exchange correlation potential. The exchange-correlation energy is taken from the known results of the many-electron interactions in an electron system of constant density (homogeneous electron gas). The exchange-correlation energy of the total molecule or solid is the integral over the contributions from each volume element. LDA is based upon two basic assumptions; the first being that exchange and

correlation effects are mainly from the immediate locality of point r and the second being that these exchange and correlation effects are slightly independent on the alteration of the electron density in the locality of r [29]. The fulfilment of these two conditions results in the same contribution from the volume element dr as if this volume element was surrounded by a constant electron density $\rho(r)$ of the same value within dr. For this study we have utilised the LDA+U method which has been widely implemented to correct the approximate DFT xc functional. The LDA+U method works in the same way as the standard LDA method to describe the valence electrons. However, for the strongly correlated electronic states (d and f orbitals), the Hubbard model is implemented for a more accurate modelling. Therefore, the total energy of the system (E_{LDA+U}) is typically the summation of standard LDA energy functional (E_{Hub}) for all the states and the energy of the Hubbard functional that describes the correlated states. Based on the simplified $LDA + U$ form, it has been customary to utilise the effective U parameter as shown in equation 2-18, instead of the interaction U parameter.

$$U_{eff} = U - J \tag{2-18}$$

Where the $"J"$ parameter is known as the exchange interaction term which accounts for Hund's rule coupling.

2.3.2. Generalized gradient approximation

Gradient-corrected density functional as suggested by Perdew [30], Becke [31], Wang [32] and Perdew, Burke and Ernzerhof [33] offer a remedy to the LDA discussed above. The basic idea with these schemes is the inclusion of terms in the exchange-correlation expressions that depend on the gradient of the electron density and not only on its value at each point in space. Therefore, these corrections are also sometimes referred to as "non-local" potentials. Table 2.1 gives the form suggested by Becke (1988) for the exchange part and Perdew (1986) for the correlation. Energies are given in Hartree atomic units; the units for the electron and spin

densities are number of electrons / (Bohr radius)^3. The constant b in Becke's formula is a parameter fitted to the exchange energy of inert gases. The explicit form of the functions f and g in Perdew's expression for the correlation energy is given in the original paper by Perdew [33]. While dissociation energies calculated with these corrections rival in accuracy the best post-Hartree-Fock quantum chemistry methods, gradient corrected density functional calculations are computationally much less demanding and more general. Gradient corrected density functionals have been studied extensively for molecular systems, for example by Andzelm and Wimmer [34].The results are very encouraging and this approach could turn out to be of great value in providing quantitative thermochemical data. The one-particle eigenvalues obtained from the gradient-corrected exchange-correlation potentials are not significantly different from the LDA eigenvalues. Therefore, these potentials do not (and are not intended to) remove the discrepancy between calculated and measured energy band gaps.

Table 2. 1 Gradient-correction to the total energy for exchange by Becke and correlation by Perdew.

$$E_{GGA} = E_{LSD} + E_x^G + E_c^G$$

Becke (1988) Gradient-corrected exchange	$E_x^G = b\sum_\sigma \int \frac{\rho_\sigma x^2{}_\sigma}{1+6bx_\sigma \sinh^{-1} x_\sigma} dr$ $x_\sigma = \frac{\lvert\nabla\rho\rvert}{\rho_\sigma^{4/3}} \qquad \sigma = \uparrow or \downarrow$
Perdew (1986) Gradient-corrected correction	$E_c^G = \int f\left(\rho_{\uparrow,}\rho_\downarrow\right) e^{-g(\rho)\lvert\nabla\rho\rvert} \lvert\nabla\rho\rvert^2 dr$

The use of GGA has little influence on local properties and tends to overestimate the bond lengths and cell parameters, but does lead usually to a significant improvement in global changes in the total energy, such as those that result when two atoms combine to make a molecule. In this work, we used the Perdew Burke Ernzerhof [33] form of the LDA+U, which was designed to be more robust and accurate for metallic systems.

2.4. Plane-wave pseudopotential method

2.4.1. Plane-waves and pseudopotentials

Plane-waves and pseudopotentials are hallmark method of calculating the electronic and atomic structures of interfaces, and they also form a very natural alliance. They are so fundamental that their strength and weakness deserve special attention. In plane-waves pseudopotential method, the model system is constructed in 3D periodic supercell which allows Bloch's theorem to be applied to the electron wave-functions:

$$\Psi_{n,k}(r) = u_{n,k}(r)^{ikr} \tag{2-19}$$

The function $u(r)$ has the periodicity of supercell. It can be of any suitable mathematical form and usually one chooses a series expansion in terms of a set of basis function. Plane-waves are used for this expansion, so that each single-electron wave-function Ψ_{nk} is written as follows.

$$\psi_{n,k}(r) = \sum u_{n,k}(G) e^{\left(i(k+G).r\right)} \tag{2-20}$$

The μ_{nk} are the expansion coefficients. The wave-vectors G are such that the plane-waves are commensurate with the supercell. Both the number of G-vectors in the sum and the number of $k's$ considered should in principle be infinite. The exponential term is a plane-waves of wave-vector k which must be commensurate with the entire system (i.e. not just the periodically-replicated cell). For an infinite system there is an infinite number of k vectors, at each of which

solutions for Ψ_{nk} exist. This simply reflects the fact that the number of electrons is infinite. However, a great simplification comes about when one realises that the change in Ψ_{nk} with k becomes negligible for k-points that are close together. This means that one may calculate at a finite number of k-points. We speak of this idea as k-point sampling. The set of vectors $\{G\}$, on the other hand, should in principle be infinite to obtain an exact representation of the wave-function. This is never necessary because summing over a finite number of G's will yield sufficient accuracy. Plane-waves basis set has many advantages such as; unbiased, completeness, single convergence criterion, mathematical simplicity and their derivatives are products in *k*-space and independence of atomic positions. On the other hand, they have disadvantages such that number of plane-waves needed being determined by the greatest curvature of the wave-function and empty space has the same quality of representation and cost a regions of interest. The advantages speak for themselves, for example the first three indicate that one can always ensure that the basis set is adequate for a calculation by increasing the number of plane-waves until the quantity of interest stops changing. In other words, the quality of the basis set depends on a single parameter, usually expressed as the energy of free electron whose wave-function has the same wave-vector as the largest wave-vector in the plane-wave basis.

$$E_c = \frac{\hbar^2 (G+k)^2}{2m} \tag{2-21}$$

All plane-waves of 'energy' less than the cut-off energy E_c are used in the expansion. The mathematical simplicity of plane-waves means the method is easier to implement, crucially so for the calculation of ionic forces which adds little complexity or cost to the calculation. Equally important in this context is the origin-less nature of plane-waves. Their independence from atomic positions means that the forces do not depend on the basis set—there are no 'Pulay' or 'wave-function' forces [35]. Even more important, new developments are easiest in

plane-wave codes. An idea to calculate a property is most rapidly realised in a plane-wave basis and even if other methods catch up in time, the plane-wave approach remains as the reference. From a computational viewpoint the first of the disadvantages appears to be very serious.

2.4.2. Pseudopotential approximation

The rapid oscillations of the wave-functions near to the nucleus, due to the very strong potential in the region and the orthogonality condition between different states, mean that a very large cut-off energy and hence basis set would be necessary. Fortunately, the study of physics and chemistry shows that the core electrons on different atoms are almost independent of the environment surrounding the atom and that only the valence electrons participate strongly in interactions between atoms. Thus, the core electron states may be assumed to be fixed and a pseudopotential may be constructed for each atomic species which takes into account the effects of the nucleus and core electrons [36]. The pseudopotential approximation allows the electronic wave-functions to be expanded using a much smaller number of plane-wave basis states. It is well known that most physical properties of solids are dependent on the valence electrons to a much greater extent than on the core electrons. The pseudopotential approximation exploits this by removing the core electrons and replace them with strong ionic potential using a weaker pseudopotential that acts on a set of pseudo wave-functions rather than the true valence wave-functions. An ionic potential, valence wave function and corresponding pseudopotential and pseudo wave functions are illustrated in figure 2.1. The valence wave-functions oscillate rapidly in the region occupied by the core electrons due to the strong ionic potential in the region. These regions maintain the orthogonality between the core wave-functions and the valence wave-functions, which is required in the Pauli's exclusion principle [37].

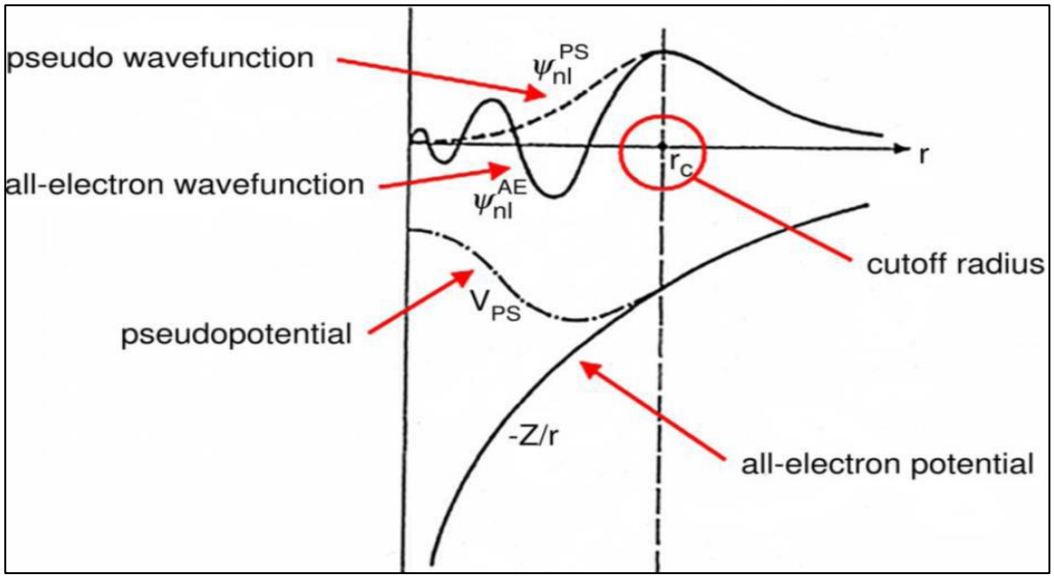

Figure 2. 1. Schematic illustration of all-electron (solid lines) and pseudo-electron (dashed lines) potentials and their corresponding wave-functions **[38]**.

The pseudopotential is constructed in such a way that its scattering properties or phase shifts for the pseudo wave-functions are identical to the scattering properties of the ion and the core electrons for the valence wave-functions, but in such a way that the pseudo wave-functions have no radial nodes in the core region. The phase shift produced by the ion core is different for each angular momentum component of the valence wave function and so the scattering from the pseudopotential must be angular momentum dependent. The most general form for pseudopotential is

$$V_{NL} = \sum_{lm} |lm\rangle V_l \langle lm| \qquad (2\text{-}22)$$

Where $\langle lm|$ are the spherical harmonics and V_l is the pseudopotential for angular momentum l. Acting on the electronic wave function with this operator decomposes the wave function into the spherical harmonics, each of which is the multiplied by the relevant pseudopotential V_l. A pseudopotential that uses the same potential for all the angular momentum components of the wave function is called a local pseudopotential. Pseudopotential is a function only of the distance from the nucleus. It is possible to produce arbitrary, predetermined phase shifts for

each angular momentum state with a local potential. However, there are limits to the amount that the phase shifts can be adjusted for the different angular momentum states while maintaining the crucial smoothness and weakness of the pseudopotential. Without a smooth, weak pseudopotential it becomes difficult to expand the wave-functions using a reasonable number of plane-waves basis states.

2.5. k-sampling

Electronic states are allowed only at a set of *k*-points determined by the boundary conditions that apply to the bulk solid. The density of allowed *k*-points is proportional to the volume of the solid. The infinite numbers of electrons in the solid are accounted for by an infinite number of *k*-points and only a finite number of electronic states are occupied at each *k*-point.

The Bloch theorem [39] changes the problem of calculating an infinite number of electronic wave-functions to one of calculating a finite number of *k*-points. The occupied states at each *k*-point contribute to the electronic potential in the bulk solid so that in principle an infinite number of calculations are needed to compute this potential. However, the electronic wave-functions at *k*-points that are very close are identical. Hence it is possible to represent the electronic wave-functions over a region of *k*-space by the wave-functions at the single k-point. In this case the electronic states at only a finite number of *k*-points are required to calculate the electronic potential and hence determine the total energy of the solid.

Methods have been devised for obtaining very accurate approximations to the electronic potential from a filled electronic band by calculating the electronic wave-functions at special sets of *k*-points. The two most common methods are those of Chadi and Cohen [40] and Monkhorst and Pack [41]. Using these methods, the electronic potential and the total energy of an insulator can be obtained by calculating the electronic states at a very small number of *k*-

points. A denser set of *k*-points are required to calculate the electronic potential and the total energy of a metallic system in order to define the Fermi surface precisely.

However, the computational cost of performing a very dense sampling of *k*-space increase linearly with the number of *k*-points in the Brillouin zone (BZ). Density functional codes approximate these *k*-space integrals with a finite sampling of *k*-points. Special *k*-points schemes have been developed to use the fewest possible *k*-points for a given accuracy, thereby reducing the computational cost. The most commonly used scheme is that of Monkhorst and Pack [41].

2.6. Plane-wave pseudopotential code

2.6.1. VASP code

Vienna *ab*-initio simulation package (VASP) is a package for performing *ab*-initio quantum-mechanical molecular dynamics (MD) using pseudopotentials and a plane-waves basis set. VASP is based on a finite-temperature local-density approximation approach (with the free energy as vibrational quantity) and an exact evaluation of the instantaneous electronic ground state at each MD-step using efficient matrix diagonalization schemes and efficient Pulay mixing [42]. These techniques avoid all problems occurring in the original Car-Parrinello method which is based on simultaneous integration of electronic and ionic equations of motion. The interaction between ions and electrons is described using ultrasoft Vanderbilt pseudopotentials (US-PP) or the projector augmented wave method (PAW) [43]. Both techniques allow a considerable reduction of the necessary number of plane-waves per atom for transition metals and first row elements. Forces and stresses can be easily calculated with VASP and used to relax atoms into their instantaneous ground state. The Projector-Augmented wave implemented in VASP reconstructs the full all-electron density and avoids the necessity of nonlinear core-corrections [44].

2.6.2. Phonon code

The computational programmes used to determine phonons are VASP, Wien2K, Phonon and etc. However, the phonon spectra can be studied within the direct method, which is implemented in the Phonon program written by Krzysztof Parlinski [45]. This method is based on the calculation of the interatomic forces in the supercell with the periodic boundary conditions. The Hellmann-Feynmann forces are obtained using one of the density functional theory codes like VASP, Wien2K or SIESTA. The direct method called Phonon code has been used to calculate the phonon dispersion curves and phonon density of states in numerous crystals, multilayers, and surfaces. Phonon code is a software for calculating phonon dispersion curves, phonon density spectra of crystals, crystals with defects, surfaces and adsorbed atoms on surfaces from either a set of force constants or from a set of Hellmann-Feynman forces calculated within an ab initio program. Phonons play an important role in solids and determine the thermal properties of all kinds of materials. They also builds a crystal structure using one of the 230 crystallographic space groups to find the force constant from the Hellmann-Feynman forces, builds the dynamical matrix, diagonalise it and calculate the phonon dispersion relations and their intensities [46]. Phonon finds the polarization vectors and the irreducible representations (Gamma point) of phonon modes and calculates the total and partial phonon density of states. It plots the internal energy, free energy, entropy, heat capacity and tensor of mean square displacements (Debye-Waller factor). Phonon finds the dynamical structure factor for the coherent inelastic neutron scattering and the incoherent doubly differential scattering cross section.

2.7 Theoretical background of the calculated properties

2.7.1 Heats of formations

The standard enthalpy of formation or standard heat of formation of a compound is the change of enthalpy that accompanies the formation of 1 mole of a substance in its standard state from its constituent elements in their standard states (the most stable form of the element at 1 bar of pressure and the specified temperature, usually 298.15 K or 25 degrees Celsius). The heats of formation and associated entropies provide a fundamental understanding on stabilities and phase diagrams construction. The results of lattice parameters and heats of formation are discussed in chapter 3. For this study, heats of formations were calculated using equation 2-23 as follows:

$$\Delta H_f\,(MCO_3) = [E_{tot} - (E_M + Ec + 3Eo)] \qquad (2\text{-}23)$$

where E_{tot} is the calculated total energy of the compound, E_M is the calculated total energy of metal element, E_C is the calculated energy of carbon, E_O is the calculated energy of oxygen in the compound. The heats of formations for all the MCO_3 structures are calculated using VASP and will be discussed in chapter 3. The heats of formations will be used for predicting the stability trend of five structures used in this study.

2.7.2 Density of states

The density of states (DOS) of a system describes the number of states per interval of energy at each energy level that are available to be occupied. DOS is a useful mathematical concept of allowing integration with respect to the electron energy to be used instead of the integration over the Brillouin zone. In other words, the density of states indicates how densely packed are quantum states in a particular system, unlike isolated systems like atoms or molecules in gas phase. A high DOS at a specific energy level means that there are many states available for

occupation, while a DOS of zero means that no states can be occupied at that energy level. In general, a DOS is an average over the space and time domains occupied by the system. In addition, DOS is often used for quick visual analysis of the electronic structure as shown in Figure 2.2. Characteristics such as the width of the valence band, the energy gap in insulators, the number and intensity of the main features are helpful in qualitatively interpreting experimental spectroscopic data. DOS analysis can also help to understand the changes in electronic structure caused by for example, external pressure.

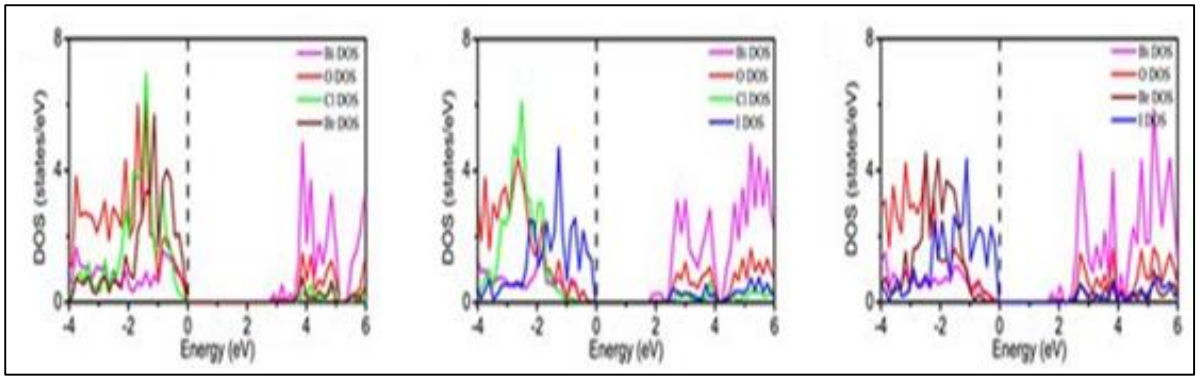

Figure 2. 2. Schematic illustration of the density of states and the fermi energy (dashed line) **[47]**.

More accurate methods are based on linear or quadratic interpolations of band energies between the reference points in the Brillouin zone. The most popular and reliable technique, which is based on the tetrahedron interpolation, is unfortunately ill suited to the Monkhorst-Pack grid of special points. Therefore, VASP uses a simplified linear interpolation scheme. This method is based on the linear interpolation in parallelepipeds formed by the points of the Monkhorst-Pack set, followed by the histogram sampling of the resultant set of band energies.

The density of states behaviour at E_f (the dashed line shown in figure 2.2) is significant and can be used to correlate their stability. It is also known from literature that the DOS for structures of the same composition can be used to mimic the stability trend with respect to their behaviour at the E_f. The structure with the highest and lowest density of density at E_f is

considered the least and most stable, respectively. Furthermore, we can determine whether our structures are metal, semi-conductors or insulators by measuring their band gaps respectively.

2.7.3 Phonon dispersion curves

The phonon dispersion curves are defined as the wave vector (k) dependence of the frequencies $\omega(k,j)$ of the normal modes for all branches and selected directions in the crystal. Phonon dispersion curves have an essential role in several physical properties of condensed matter physics. These include thermal conductivity, mechanical stability and electrical conductivity. They indicate an excited state in the quantum mechanical quantization for the modes of vibrations of elastic structures of interacting particles. The behaviour of phonon dispersion branches reflects specific features of the crystal structure and the interatomic interactions and therefore gives the most comprehensive and detailed information about the dynamical properties of crystals.

In crystals were there are two or more types of atoms, two types of vibrations are displayed; acoustic and optical. Optical phonons arise from out of phase vibrations between neighbouring atoms within the unit cell, while the in phase vibrations give rise to acoustic phonons. The acoustic modes have zero frequencies at Γ (centre of the Brillouin zone) while optical modes have non-zero. The acoustic and optical split into longitudinal and transverse modes abbreviated as longitudinal acoustic (LA), transverse acoustic (TA), longitudinal optical (LO) and transverse optical (TO), also the out-of-plane acoustic (ZA) and out-of-plane optical (ZO) as shown in figure 2.1. A linear relationship between frequency and long wavelengths phonon wave-vector is displayed in acoustic mode. Negative vibrational frequencies (soft modes) indicate mechanical instability of the system, while positive vibrations show stability. Along with the Γ point (centre of the Brillouin zone) there are several points of high symmetry which are of significant interest. Table 2.2 lists and describes the critical k-points of high symmetry

line in the first Brillouin zone for certain Bravais lattice of base centred cubic (BCC), face centred cubic (FCC), and hexagonal lattices [48].

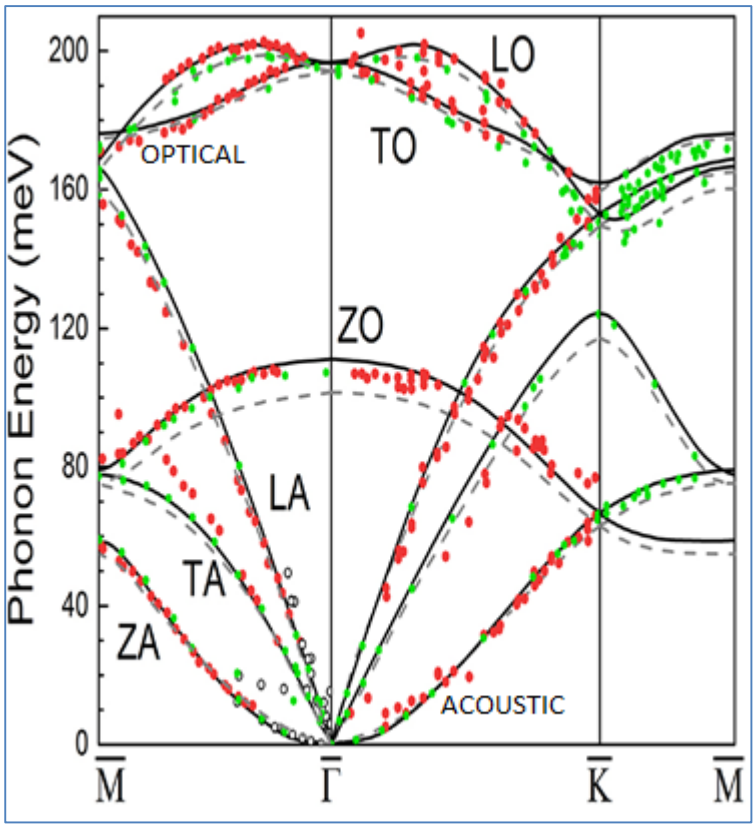

Figure 2. 3. Illustration of the optic and acoustic phonon modes [49].

Table 2. 2. Analysis of the critical k-points in the Brillouin zone.

Simple Cube	
Symbol	**Description**
$\Gamma(0,0,0)$	Centre of the Brillouin zone
$M(1/2,1/2,0)$	Centre of an edge
$R(1/2,1/2,1/2)$	Corner point
$X(0,1/2,0)$	Centre of a face
Body-centred cubic	
Symbol	**Description**
$H(-1/2,1/2,1/2)$	Corner point joining four edges

P(1/4,1/4,1/4)	Corner point joining three edges
N(0,1/2,0)	Centre of a face
Face-centred cubic	
Symbol	**Description**
K(3/8,3/4,3/8)	Middle of an edge joining two trigonal faces
L(1/2,1/2,1/2)	Centre of a trigonal face
U(1/4,5/8,5/8)	Middle of an edge joining a trigonal and a square face
W(1/4,3/4,1/2)	Corner point
X(0,1/2,1/2)	Centre of a square face
Hexagonal	
Symbol	**Description**
A(0,0,1/2)	Centre of a hexagonal face
K(2/3,1/3,1/2)	Middle of an edge joining two rectangular faces
H(1/2,0,0)	Corner point
L(1/2,0,1/2)	Middle of an edge joining a rectangular and a hexagonal face
M(1/2,0,0)	Centre of a rectangular face

2.7.4. Theory of elasticity

From the perspective of material physics, the elastic constants C_{ij}, contains important information that can be obtained from ground-state total-energy calculations. A given crystal structure cannot exist in a stable or metastable phase unless its elastic constants obey certain relationships. The C_{ij} also determines the response of the crystal to external forces, as characterized by the bulk modulus, shear modulus, Young's modulus and Poisson's ratio and so play an important role in determining the strength of a material [50]. First-principles calculations that use periodic boundary conditions assume the existence of a single crystal, so

all elastic constants can be determined by direct computation. The calculated C_{ij} can then be used to check the experimental bulk and shear moduli, if available and to calibrate model calculations. In addition, the elastic constants can be used to check the phase stability of proposed compounds [51]. First-principles calculations can thus be used to predict the existence and properties of new materials.

2.7.5. Definition of elastic constants

To determine the elastic constants of a crystal, a deformation of the unit cell is created by changing the Bravais lattice vectors R = (a, b, c) of the undisturbed unit cell to R′ = (a', b', c') using a strain matrix e below;

$$R' = R.\begin{pmatrix} 1+e_{xx} & \frac{1}{2}e_{xy} & \frac{1}{2}e_{xz} \\ \frac{1}{2}e_{yx} & 1+e_{yy} & \frac{1}{2}e_{yz} \\ \frac{1}{2}e_{zx} & \frac{1}{2}e_{zy} & 1+e_{zz} \end{pmatrix}. \qquad (2\text{-}24)$$

The deformation leads to a change of the total energy of the crystal

$$U = \frac{E_{tot} - E_0}{V_0} = \frac{1}{2}\sum_{i=1}^{6}\sum_{j=1}^{6} C_{ij} e_i e_j \qquad (2\text{-}25)$$

where E_0 is the total energy of the unstrained lattice, V_0 is the volume of the undistorted cell and C_{ij} are the elements of the elastic constant matrix with a notation that follows standard convention. Both i and j run from 1…6 in the sequence {xx, yy, zz, yz, xz, xy}. The tensor of elasticity has 36 elements, the elastic constants, but maximally 21 of these are independent.

2.7.6. Calculation of elastic constants

The simplest case by far is the cubic system where there are only three independent constants,C_{11}, C_{12} and C_{44}. We use this case to illustrate the manner in which the stiffness

matrix elements may be determined from strain fields of the form (2-22). If the applied strain is $e_{xx} = e$ with all other e_i equal to zero, the energy change is $U = \frac{C_{44}e^2}{2}$. This allows a unique determination of C_{11}. If $e_{yz} = e_{zy} = \frac{e}{2}$, with all other strain components zero, then $U = \frac{C_{44}e^2}{2}$ and we have an independent determination of C_{44}. The bulk modulus B, is the response to a uniform compression so applying the strain field $e_{xx} = e_{yy} = e_{zz} = e$ allows the computation of B via the relation $U = \frac{Be^2}{2}$. Similarly, the shear modulus can be calculated by using the strain field $e_{zz} = e_{xx} = e_{yy} = -\frac{e}{2}$, whereupon $U = \frac{3c\prime e^2}{2}$. Finally, the off-diagonal stiffness matrix element C_{12} can be calculated using one or other of the relations as shown below.

$$B = \frac{1}{2}(C_{11} + 2C_{12}) \tag{2-26}$$

$$C' = \frac{1}{2}(C_{11} - C_{12}) \tag{2-27}$$

Using both of these relations provides a useful independent check on the accuracy of the computation. A symmetry-general formulation of the calculation of elastic constants from total energy calculations is given by Le Page and Saxe [52].

2.7.7 Elastic constant stability conditions

The accurate calculation of elasticity is essential for gaining an insight into the mechanical stability and elastic properties of solids. For the cubic, tetragonal, orthorhombic and trigonal crystals, there are three (C_{11}, C_{12}, C_{44}), six (C_{11}, C_{12}, C_{13}, C_{33}, C_{44}, C_{66}) thirteen (C_{11}, C_{22}, C_{33}, C_{12}, C_{13}, C_{23}, C_{44}, C_{55}, C_{66}, C_{15}, C_{25}, C_{35}, C_{46}) and six/seven (C_{11}, C_{33}, C_{44}, C_{12}, C_{13}, C_{14}) or (C_{11}, C_{33}, C_{44}, C_{12}, C_{13}, C_{14}, C_{66}) independent elastic constants. Applying two kinds of strains (ε_1 and ε_4) can give stresses relating to these elastic coefficients, yielding an efficient method for obtaining elastic constants for the cubic system. This method has been successfully used to

study the elastic properties of a range of materials including metallic systems [50]. The mechanical stability criteria of cubic systems as outlined elsewhere [53] are shown below;

$$C_{11} - C_{12} > 0;\ C_{11} + 2C_{12} > 0;\ C_{44} > 0 \tag{2-28}$$

where C_{11}, C_{12} and C_{44} are the only three independent elastic constants. Based on three independent single crystal elastic constants of a cubic crystal, C_{11}, C_{12}, C_{44}, the elastic moduli are determined using the following expressions:

$$B = \left(\frac{C_{11} + 2C_{12}}{3}\right),\ C' = \frac{C_{11} - C_{12}}{2},\ A = \frac{(2C_{44} + C_{12})}{C_{11}}, \tag{2-29}$$

where B is the bulk modulus, C' tetragonal shear modulus and anisotropic factor A. It is acknowledged that the bulk modulus B is a measure of resistance to volume changed by applied pressure, whereas the elastic anisotropy A has an important implication in engineering science since it is highly correlated with the possibility of inducing micro-cracks in materials [53]. If the material is completely isotropic, the value of A will be 1, while values smaller or larger than 1 measure the degree of elastic anisotropy. The positive C' indicates the mechanical stability of the crystal, while the negative C' indicate the mechanical instability.

CHAPTER 3

Ab initio Studies of MCO_3

In this chapter we discuss the *ab initio* first principles results for five transition metal carbonates (MCO_3) under the study. We particularly discuss their equilibrium lattice constants, heats of formations, band structures (BS), density of states (DOS), elastic properties and phonon dispersion curves. The equilibrium lattice parameters are compared with the experimental data available to validate the approach employed. The calculations were performed using DFT+U approach as implemented in the Vienna Ab initio simulation Package (VASP) code [54]. The projector augmented wave (PAW) [55, 56] potential sets were employed with the exchange and correlation functional approximated in the spin-polarised localised density approximation (LDA) with Hubbard (U) parameter correction [57]. A U parameter of 5.5eV was employed for $FeCO_3$, $CoCO_3$ and $NiCO_3$, while a value of 4.5eV was used for $MnCO_3$.

3.1 Energy Convergence

3.1.1 Cut-off energy

To determine the appropriate cut-off energy for MCO_3 structures, single point energy calculations were performed for different kinetic energy cut-offs varied from 200 to 800eV at default number of *k*-points for each system. A cut-off energy value of 500eV was found to successfully converge the total energy of all MCO_3 structures to within 1meV. As shown in Figure 3.1, the convergence curves of total energy versus cut-off energy for MCO_3 become relatively constant from 500eV, hence it was used as a cut-off energy for all the calculations performed in the study.

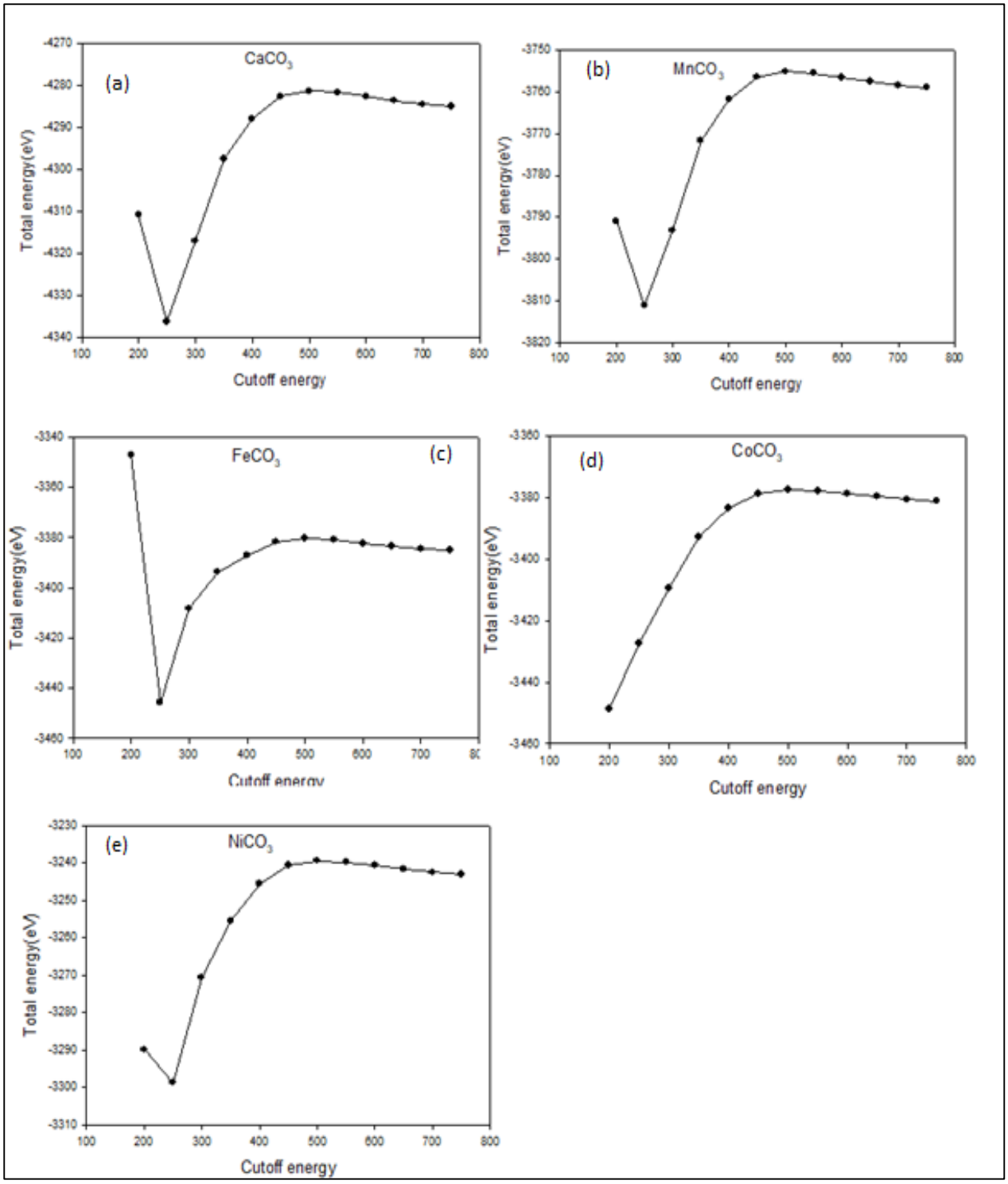

Figure 3. 1 Total convergence energy Vs cut-off energy for (a) $CaCO_3$, (b) $MnCO_3$, (c) $FeCO_3$, (d) $CoCO_3$ and (e) $NiCO_3$

3.1.2 *k*-points sampling

In order to determine the correct k-mesh parameters for Brillouin zone sampling, we have calculated the total convergence energy with respect to the k-mesh sampling set size. The k-

mesh parameters were varied from 1x1x1 to 8x8x8. As shown in figure 3.2, a *k*-mesh sampling of 4x4x4 is sufficient to successfully converge the total energy of all MCO_3 structures to within 1meV, since the total energy is relatively constant from a k-mesh of 4x4x4.

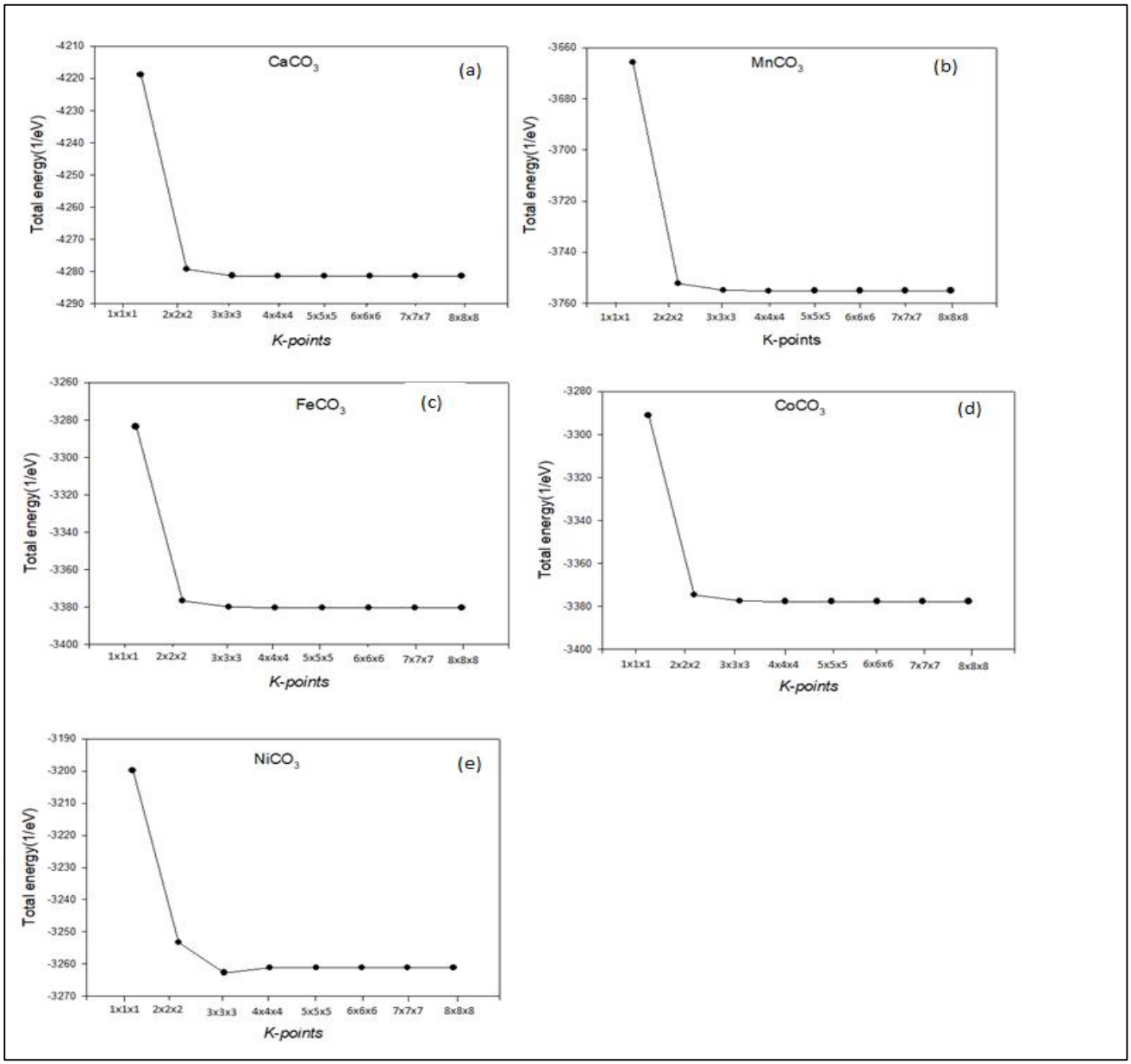

Figure 3. 2 Total convergence energy Vs k-mesh parameters for (a) $CaCO_3$, (b) $MnCO_3$, (c) $FeCO_3$, (d) $CoCO_3$ and (e) $NiCO_3$.

3.2. Energetic properties

In Table 3.1, we present the calculated LDA+U equilibrium lattice constants and heats of formations for all MCO_3 structures considered for the study. The equilibrium lattice parameters were obtained by performing full relaxation of cell volumes and atomic positions. Our

calculated lattice parameters are in good agreement with the reported experimental values for all MCO_3 structures, suggesting validity of the approach employed. Furthermore, we note that the equilibrium cell volume decreases with an increase in atomic weight of the transition metals, while the density increases with the atomic weight of the transition metals. This suggests that $NiCO_3$ has greater resistance to compressibility compared to $CoCO_3$, $FeCO_3$, $MnCO_3$ and $CaCO_3$ respectively. In order to determine the thermodynamic stability, we have calculated the heats of formation using equation number 3-1;

$$\Delta H_f(kJ/mol) = \frac{1}{N}[E_{tot} - (E_M + E_C + 3E_O)] \quad (3\text{-}1)$$

where N is the number of atoms, E_{tot} is the total energy of the compound MCO_3, while E_M, E_C and E_O are the ground state energies for M, C and O, respectively. The lower the heats of formation, the more stable is the system. We note that our calculated heats of formations are relatively low and negative, suggesting thermodynamic stability of all systems. Furthermore, the negative heats of formations indicate that the considered MCO_3 systems can be formed experimentally. Moreover, the heats of formations were found to be increasing with the transition metals and hence the stability trend is as follows:

$$CaCO_3 > MnCO_3 > FeCO_3 > NiCO_3 > CoCO_3 \quad (3\text{-}2)$$

To the best of our knowledge, no experimental heats of formation data has been reported for the considered MCO_3 systems for comparison, hence our calculated values can be used for benchmarking in future.

Table 3. 1 Calculated and experimental lattice parameters and heats of formation for MCO_3 structures.

	$CaCO_3$	$MnCO_3$	$FeCO_3$	$CoCO_3$	$NiCO_3$
a (Å)	5.162	4.846	4.732	4.708	4.634
Exp.	4.989[a]	4.776[a]	4.668[b]	4.659 [a]	4.612[c]
c (Å)	17.711[a]	15.825	15.207	15.000	14.785
Exp.	17.044 [a]	15.690[a]	15.372 [b]	14.989 [a]	14.735 [c]
V ($Å^3$)	411.322	321.849	294.842	287.967	274.999
Exp.	367.320[a]	309.910[a]	292.570[b]	281.670[a]	271.400[c]
ΔH_f (kJ/mol)	-1030.902	-704.13	-583.246	-530.158	-536.488
Density (mg/m^3)	2.424	3.558	3.915	4.115	4.300

[58][a] [59][b] [60][c]

3.3. Electronic properties

3.3.1 Band structures

In this section we present and discuss the calculated electronic band structures (BS) and densities of states (DOS) for MCO_3 systems. Electronic band structures are plots of energy versus wave-vectors for a number of bands. They help in determining if the material is an insulator, semiconductor or conductor/metal by defining the size of the energy band gaps around the Fermi level. An energy band gap is the distance between the valence band and the conduction band of electrons.

In Figure 3.3, we present the electronic band structures for five MCO_3 structures under the study. As shown in Figure 3.3(a), the band structure plot for $CaCO_3$ shows the energy band gap of 4.824eV along high symmetry lines Γ (0,0,0) and L(1/2,1/2,1/2), suggesting that the system is an insulator. The valence maximum is located near the middle of an edge joining a trigonal face at -0.071eV while the conduction band minimum is located near the centre of the Brillouin zone (Γ) at 4.754eV with respect to the Fermi level. Similarly, to $CaCO_3$ and $MnCO_3$ (Figure

3.3(b)) shows energy band gap of 3.526eV indicating an insulator behaviour. The insulator behaviour characteristic is not desirable for our study since insulators cannot conduct electricity and hence not suitable for cathode materials. The valence band maximum for $MnCO_3$ is located at -0.058eV while the conduction band minimum is located at 3.468eV with respect to the Fermi level.

Contrary to $CaCO_3$ and $MnCO_3$, we note that the lightly denser $CoCO_3$ and $NiCO_3$ systems show energy band gaps of 2.640eV and 2.518eV suggesting semiconductor behaviour and hence improved electronic conductivity. Their respective valence band maxima are located at -0.068eV and -0.067eV while the conduction band minima are at 2.572eV and 2.451eV, respectively. To the good interest of this study, $FeCO_3$ band structure plot display no energy band gap at the Fermi level, suggesting metallic characteristic and good electronic conductivity. As shown in Figure 3.3(c), there is an overlap between the valence conduction band states around the Fermi level.

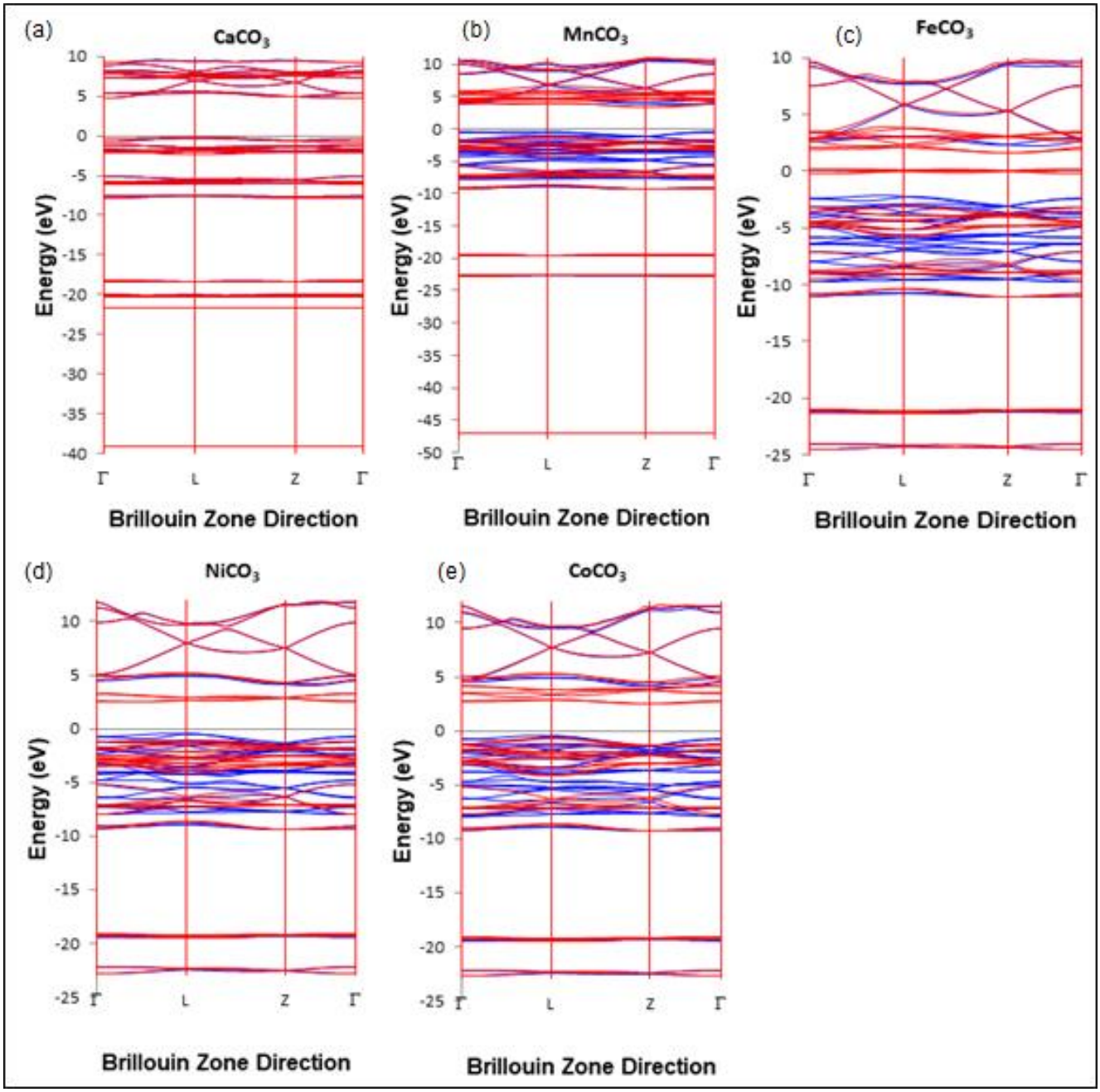

Figure 3. 3 Band structure for MCO_3 structures used in this study

3.3.2 Density of states

Density of states (DOS) is referred to as the energy levels that can be occupied by electrons of different number of states. The density of states for structures of the same composition can be used to check the stability trend with respect to their behaviour at the Fermi level (E_f). The figures below display the total and partial density of states for MCO_3 structures under the study. The DOS calculations were computed using the spin polarised local density approximation

with Hubbard correction (U) at 0K. The top most plots in all the figures display total DOS while the subsequent lower plots display partial DOS. The spin up states are shown on the positive scale of TDOS while the spin down states are shown on the negative scale of TDOS. The total electronic contribution of whole system is indicated by the total DOS while the contributions of each individual atom is indicated by the partial DOS. Moreover, the Fermi energy is taken as the energy zero ($E - E_F = 0$) in all the plots.

Figure 3.4 (a) shows the total and partial density of states for $CaCO_3$. We note that the Fermi level is located on the edge of the valence band, and thus not permissible for valence band states to overlap to the conduction band. The location of the Fermi level suggests insulator behaviour and is in good agreement with the band structure prediction. The partial DOS plots show that the valence band states near the Fermi level are predominantly of O p-orbital with weak hybridisation of Ca and C orbitals. The peaks located between -25eV and -19eV reflect the strong hybridisation between the Ca p-states, C s-states, C p-states and O s-states while the peaks located at -6eV is due to the hybridisation of C p-states and O p-states.

In Figure 3.4 (b) we present the total and partial DOS for $MnCO_3$ system. Similarly to $CaCO_3$, we note that the Fermi level is located on the edge of the valance band, suggesting insulator behaviour. The partial DOS plots indicate that the states in the energy range of -10eV to 0eV are predominately of Mn *d*-states and O *p*-states, with minimum contribution from C *p*-states. Moreover, the peaks located at 5eV in the conduction band are a result of hybridisation of C *p*-states, Mn *d*-states and O *p*-states. Furthermore we observe two degenerate low spin Mn *3d* peaks at about 5eV, suggesting Mn^{2+} and Mn^{3+} oxidation states.

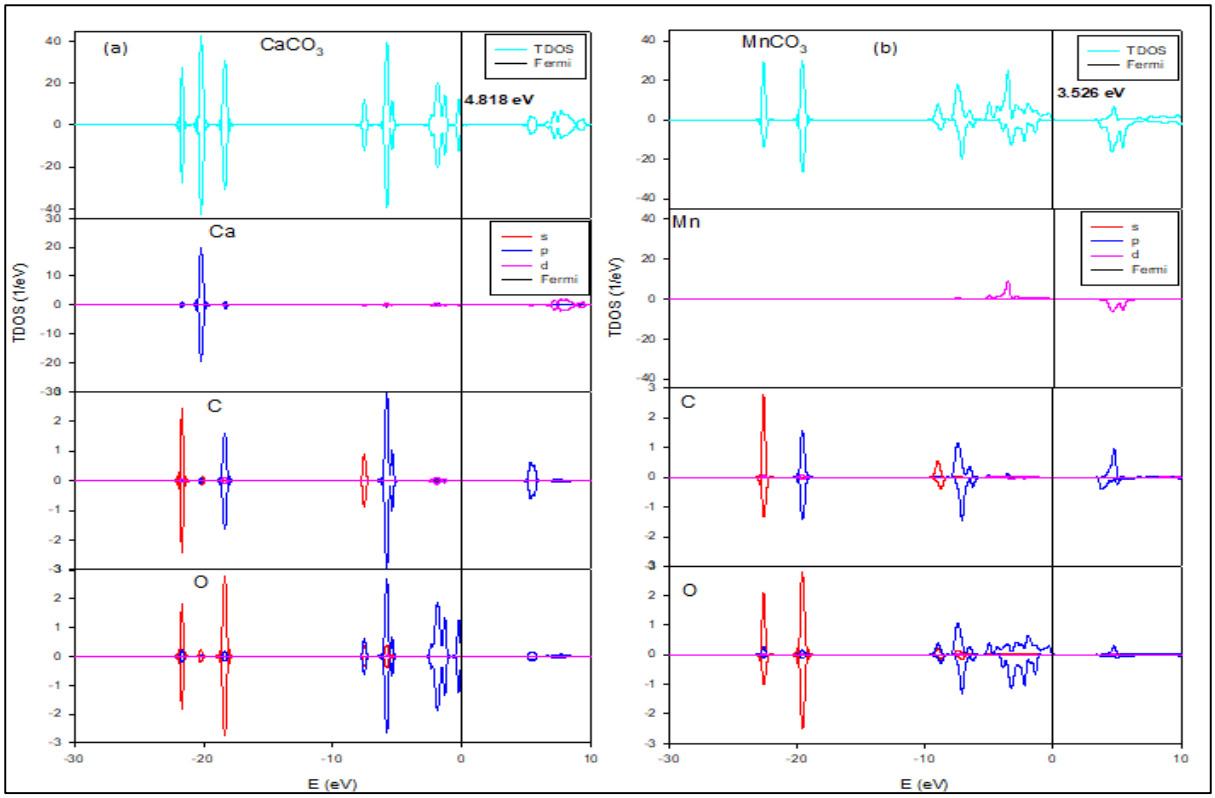

Figure 3. 4 Total and partial DOS for (a) $CaCO_3$ and (b) $MnCO_3$

Figure 3.5 presents the total and partial DOS for $FeCO_3$ and $CoCO_3$. For $FeCO_3$, we note that the Fermi level is located deep in the Fe *3d* spin down bands, implying permissibility of valence states to overlap to the conduction band. The location of the Fermi level suggests semi-metallic behaviour and good electric conduction, which correspond well with the band structure prediction. The spin up states are insulating, while the spin down states are metallic. On the other hand, $CoCO_3$ plot shows that the Fermi level is located on the edge of the valence band. However, we note a relatively narrow band gaps of 2.640eV, suggesting that the material is a semiconductor. Similarly, to $MnCO_3$, we observe that $FeCO_3$ and $CoCO_3$ show two degenerate spin down peaks in the conduction band corresponding to Fe/Co^{2+} and Fe/Co^{3+} oxidation states. The partial DOS for $FeCO_3$ shows that the states around the Fermi level are primarily of Fe *3d*-orbital with negligible contributions from O *2p* and C *3d* orbitals. On the other hand, the partial DOS for $CoCO_3$ show that the peak located in the energy range of -10eV and 0eV are mainly dominated by Co *3d*-orbital correlated by weak O *2p* and C *2p* hybridisation. Moreover, the conduction band are principally of strong hybridisation between Co *3d* and C *2p* orbitals.

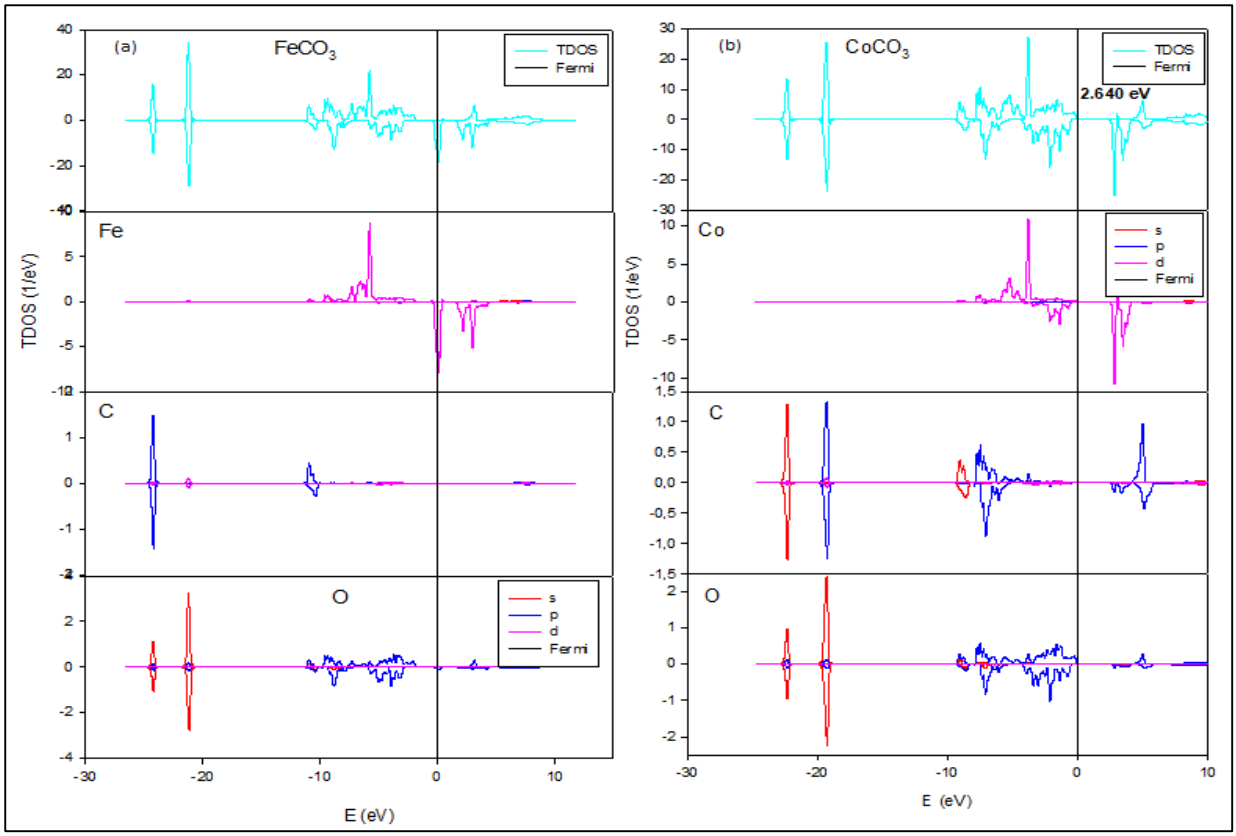

Figure 3. 5 Total and partial DOS for (a) $FeCO_3$ and (b) $CoCO_3$

Lastly, in Figure 3.6 we present the total and partial Dos of $NiCO_3$. We note that the Fermi level is located on the edge of the valence band, suggesting impermissibility of valence states to overlap to the conduction band. However, similarly to $CoCO_3$, we also note a relatively narrow band gap, suggesting semiconductor behaviour. In contrary to $MnCO_3$, $FeCO_3$ and $CoCO_3$, we note a single degenerate spin down peak in the conduction band corresponding to Ni^{2+} oxidation state.

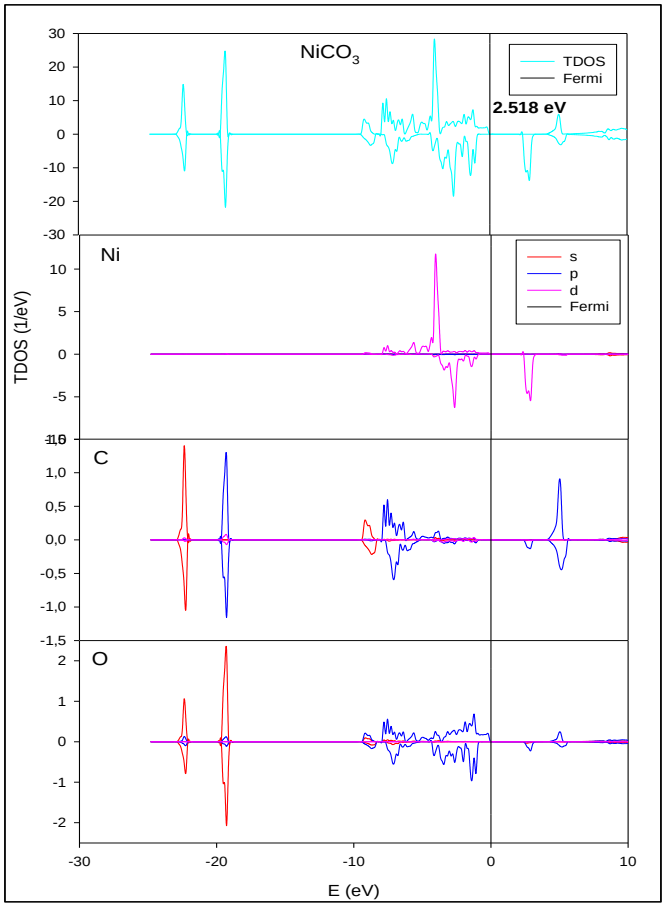

Figure 3. 6 Total and partial DOS for $NiCO_3$ structure

3.4. Elastic properties

The understanding of elastic constants, moduli and anisotropy is important since they determine the response of materials to the applied macroscopic stress. They also provide essential information on mechanical stability, stiffness, hardness, brittleness/ductility nature, susceptibility to cracks induced due to thermal expansion coefficient and nature of the forces acting in solid materials. Elastic constants (C_{ij}) were calculated by Taylor expansion of the total energy as shown below [61];

$$U(V,\varepsilon) = U(V_0,0) + V_0\left[\sum_i \tau_i\varepsilon_i\delta_i + \frac{1}{2}\sum_{ij} C_{ij}\,\varepsilon_i\delta_i\varepsilon_j\delta_i\right] \quad (3\text{-}3)$$

where $U(V_{0,}0)$ is the energy of the unstrained system with equilibrium volume were V_0, τ_i is element in the stress tensor and ξ_i is a factor to take care of Voigt index. There are six independent $(C_{11}, C_{12}, C_{13}, C_{14}, C_{33}, C_{44})$ and one dependent $(C' = C_{11} - C_{12}/2)$ elastic

constants for trigonal lattice systems. For trigonal crystal systems to be considered mechanically stable, the following necessary Born stability conditions must be satisfied [62].

$$C_{11} - |C_{12}| > 0, (C_{44} + C_{12})C_{33} - 2C_{13}^2 > 0, (C_{11} + C_{12})C_{44} - 2C_{14}^2 > 0 \quad (3\text{-}4)$$

The calculated elastic constants for MCO_3 structures are presented in Table 3.2. We note that the necessary stability condition for $CaCO_3$, $MnCO_3$, $CoCO_3$ and $NiCO_3$ are satisfied, indicating mechanical stability. Furthermore, their respective C$^{'}$ is positive, endorsing mechanical stability. On the other hand, $FeCO_3$ shows negative value of C_{12} and C_{44} and the stability conditions $(C_{44} + C_{12})C_{33} - 2C_{13}^2 > 0 \; and \; (C_{11} + C_{12})C_{44} - 2C_{14}^2 > 0$ are not satisfied, suggesting mechanical instability. From the calculated elastic constants, the macroscopic bulk (B), shear (G) and Young's (E) moduli were estimated using the Voigt-Ruess-Hill approximation method [63, 64, 65]. The Voigt and Ruess theory correspond to the upper and lower limits respectively, while the Hill theory is the average of the Voigt and Reuss respectively. The bulk (B) modulus determines the material's hardness and resistance to compression under pressure.

From our calculations as presented in Table 3.2, it can be seen that the $NiCO_3$ system possesses highest hardness over $CoCO_3$, $MnCO_3$, $FeCO_3$ and $CaCO_3$ respectively due to its largest value of the bulk modulus. The shear (G) modulus describes the response of materials to deformation against external forces. We note that $FeCO_3$ has highest shear modulus value (111.44 GPa), indicating highest resistance over $NiCO_3$, $CoCO_3$, $MnCO_3$ and $CaCO_3$ respectively. It is interesting to note that shear modulus is greater than bulk modulus in $FeCO_3$. This means that $FeCO_3$ has greater stiffness than hardness and resistance to deformation, thus greater susceptibility cracks when subjected under pressure. In the other systems, the bulk is greater than the shear implying that shear modulus is the parameter limiting stability. The Young modulus (E) which determines stiffness of materials showed that $FeCO_3$ possesses greater

stiffness over $NiCO_3$, $CoCO_3$, $MnCO_3$ and $CaCO_3$ respectively. In order to determine the brittleness and ductility nature of MCO_3 materials, we have calculated the B/G ratio as proposed by Pugh [66]. Materials are considered ductile if the Pugh ratio value is greater than 1.75 and brittle if less than 1.75. We note that our calculated B/G ratio values are greater than 1.75 for $MnCO_3$ and $CoCO_3$, suggesting ductility (i.e. the ability to bend without deformation). On the other hand, the Pugh ratio values for $CaCO_3$, $FeCO_3$ and $NiCO_3$ are less than 1.75, suggesting brittleness (i.e. structural deformation after bending). Moreover, it is of interest to note that $FeCO_3$ shows a very low ratio of 0.5118, which suggests greater deformation in this material. The low ratio emanates from the fact that the shear modulus is highly greater than the bulk modulus.

The materials anisotropies were calculated by making use of the universal elastic anisotropy (A^U) which quantifies single crystal elastic anisotropy. Anisotropy factors are essential to determine the susceptibility of materials to cracks and in reducing micro-cracks and dislocation [67]. The universal elastic anisotropy index is defined by equation 3-5 below;

$$A^U = 5\frac{G^V}{G^R} + \frac{B^V}{B^R} - 6 \qquad (3\text{-}5)$$

where G is the shear modulus, B is the bulk modulus and the superscripts V and R denote the Voigt and Reuss bounds respectively for the ensemble averaged quantities over the crystal. For isotropic crystals, $A^U = 0$ while larger values of A^U indicate stronger anisotropy. The calculated A^U values are less than 1 for $CaCO_3$, $MnCO_3$, $CoCO_3$ and $NiCO_3$ suggesting nearly isotropic behaviour. On the other hand, $FeCO_3$ shows larger value of A^U which indicate that this system possesses highest anisotropy, hence greatest susceptibility to cracks.

Moreover, Chung and Buessem [68] have introduced the percent anisotropy factors for bulk modulus (A_B) and the shear modulus (A_G) to measure the crystal anisotropy which is defined as follows:

$$A_B = \frac{B_V - B_R}{B_V + B_R} \tag{3-6}$$

$$A_G = \frac{G_V - G_R}{G_V + G_R} \tag{3-7}$$

where B_V, B_R, G_V and G_R are the bulk and shear modulus estimation within Voight and Reuss methods. For an isotropic crystal, the values of A_B and A_G must be zero. We note that the percentage anisotropy (A_B and A_G) for $CaCO_3$, $MnCO_3$, $CoCO_3$ and $NiCO_3$ are less than 0.08, endorsing nearly isotropic behaviour. $FeCO_3$ has a A_B and A_G values of 0.36 and 0.79 respectively, further suggesting greatest susceptibility of cracks. The percentage shear modulus anisotropy A_G is greater than the percentage bulk modulus anisotropy A_B; thus these systems are less in compressibility than in shear [69].

Table 3. 2. Calculated elastic constants, moduli, Pugh ratio and anisotropy for $CaCO_3$, $MnCO_3$, $FeCO_3$, $CoCO_3$ and $NiCO_3$ structures. Experimental data is presented in parenthesis.

C_{ij} (GPa)	$CaCO_3$	$MnCO_3$	$FeCO_3$	$CoCO_3$	$NiCO_3$
C_{11}	125.57 (148.0)[a]	204.96(223.9)[a]	703.63	242.95	277.45 (217.8)[b]
C_{12}	40.73 (55.4)[a]	70.83(93.4)[a]	-588.1	86.96	78.91 (51.87)[b]
C_{13}	30.07 (54.5)[a]	63.16(76.0)[a]	82.41	66.62	64.21 (97.93)[b]
C_{14}	12.03 (-20.8)[a]	14.58(–17.3)[a]	101.32	15.56	16.70 (27.60)[b]
C_{33}	68.06 (85.7)[a]	115.72(132.6)[a]	135.88	145.33	157.07(298.99)[b]
C_{44}	31.44 (32.8)[a]	41.95(44.5)[a]	-152.8	48.92	59.53 (82.69)[b]
C'	105.21	169.55	997.68	199.47	237.18
B_V	57.88	102.22	77.39	120.06	125.18
B_R	52.21	94.02	36.68	109.20	115.38

B_H	55.05	98.12	57.04	114.63	120.28
G_V	35.61	52.10	199.14	62.34	77.31
G_R	31.10	45.68	23.75	55.52	69.31
G_H	33.36	48.89	111.44	58.93	73.31
E_V	88.66	133.59	321.59	159.44	192.33
E_R	77.85	117.95	58.60	142.43	173.24
E_H	83.25	125.77	190.09	150.93	182.78
$\frac{B}{G}$	1.6402	2.0069	0.5118	1.9451	1.6407
A^U	0.830	0.790	38.030	0.710	0.660
$A_B(\%)$	0.05	0.04	0.36	0.05	0.04
$A_G(\%)$	0.07	0.07	0.79	0.06	0.05

[a] [70] [b] [71]

3.5. Phonon dispersion curves

The study of phonons is an important part of solid state physics, since phonons play a major role in many physical properties of the solids, including materials thermal conductivity. In particular, the properties of long-wavelength phonons give rise to sound in solids [72]. Phonons are quantum mechanical version of a special type of vibrational motion, known as normal modes in classical mechanics, in which each part of a lattice oscillates with the same frequency. Furthermore, phonon dispersion curves give information on the elementary vibrations of the lattice. The phonon dispersion spectrum is used to draw an analogy between photon representing a quantum of electromagnetic radiation and quanta of lattice vibration. Theory of phonons explains most solid state phenomena, such as specific heat, melting, stability, thermal and electrical conductivity, etc., which cannot be explained with static lattice theory [73]. Hence, in order to investigate the vibrational stability of the transition metal carbonates

(MCO_3), we have calculated their phonon dispersion curves along symmetry direction within their respective first Brillouin zones. When analysing the phonon dispersion curves, structures are said to be stable if there are no negative frequencies (referred to as soft modes) along high symmetry directions.

The phonon dispersion curves for MCO_3 structures were calculated using the PHONON code by Parlinski [74] as implemented in MedeA software, which allows phonon dispersion curves and thermodynamic properties such as vibrational heat capacity at constant volume, vibrational internal energy, entropy and free energy to be calculated. The supercell was constructed from the hexagonal cell with the interaction range of 10.0Å and the displacement of +/-0.06Å during the phonon dispersion curve calculations. The PHONON code allows for calculation of lattice dynamics, dispersion curves and phonon density spectra of crystals from either a set of force constants or from a set of Hellmann-Feyman forces computed within an ab initio program which optimises the structure of the crystalline supercell within constraints imposed by a crystallographic space group [75].

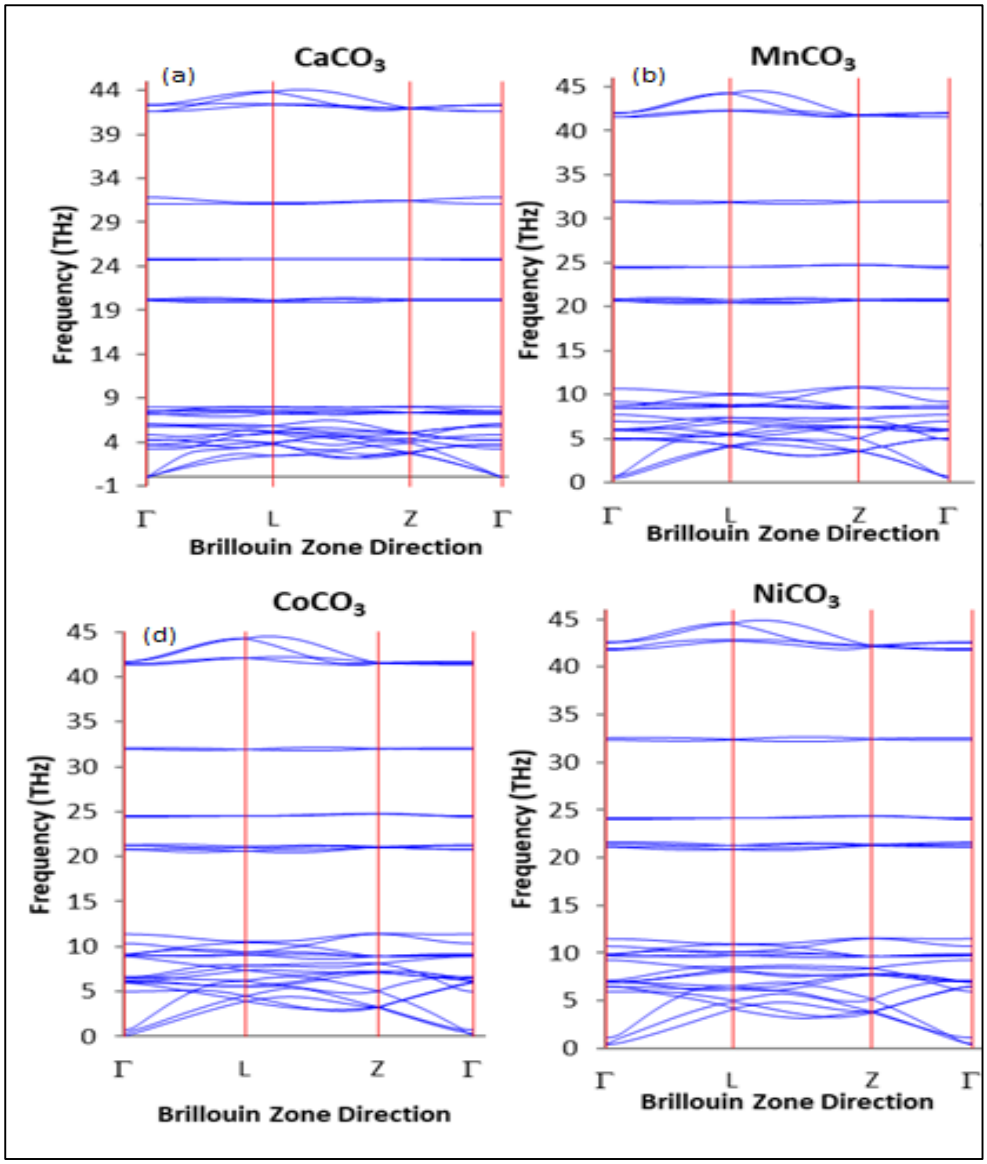

Figure 3. 7. Phonon dispersion curves for (a) $CaCO_3$, (b) $MnCO_3$, (c) $FeCO_3$, (d) $CoCO_3$ and (e) $NiCO_3$ along high symmetry lines in the Brillouin zone.

The phonon dispersion curves of MCO_3 structures along high symmetry directions in the Brillouin zone are shown in Figure 3.7. Our phonon dispersion curves display both the acoustic and optical modes. In optical modes, two atoms in a unit cell vibrate in opposite direction, while atoms in the unit cell vibrate along the same direction for acoustic modes. The lower curve is for acoustic branches and it begins at $q = 0\ and\ \omega = 0$, while the upper curve is called the optimal branch whereby q and w represents wave vector and angular frequency respectively. The phonon dispersion curves for $CaCO_3$, $MnCO_3$, $NiCO_3$ and $CoCO_3$ are quite similar, suggesting analogous electronic structure of the outmost shell for their respective

transition metals. Moreover, we note the presence of the phonon band gap between the acoustic and optical branches for $CaCO_3$, $MnCO_3$, $NiCO_3$ and $CoCO_3$ indicating similarity in their atomic masses [76, 77]. Furthermore, we note that the phonon dispersion spectra for $CaCO_3$, $MnCO_3$, $NiCO_3$ and $CoCO_3$ display modes with only positive frequencies, suggesting vibrational stability. On the other hand, the phonon dispersion spectrum and for $FeCO_3$ display the availability of soft modes along the high symmetry directions Γ, L, Z which indicate vibrational instability. Our calculated phonon dispersion curves are consistent with the calculated elastic properties, where $CaCO_3$, $MnCO_3$, $NiCO_3$ and $CoCO_3$ were predicted to be mechanically stable while $FeCO_3$ mechanically unstable.

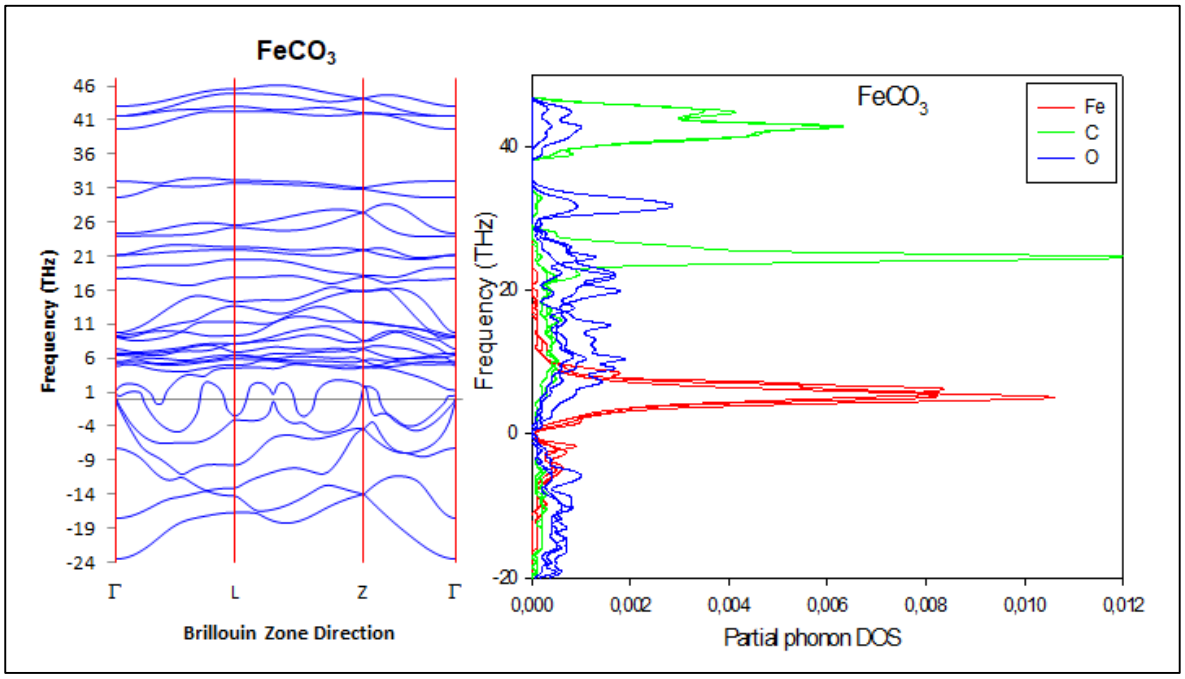

Figure 3.8. Phonon dispersion curve and partial phonon density of states (PDOS) for $FeCO_3$.

To investigate the origin of negative frequencies in $FeCO_3$, we plotted the direction-projected partial phonon density of states as predicted in Figure 3.8. The partial phonon density of states indicate as to which atoms are responsible for particular vibrations. We note that all the atoms in $FeCO_3$ have somewhat contributed to the availability of soft modes, with oxygen contributing relatively more than iron and carbon atoms, respectively. The upper soft modes

(0-7THz) are predominantly from oxygen (O), while the lower soft modes (8-20 THz) are from iron (Fe).

CHAPTER 4

Cluster expansion and Monte Carlo simulations for MCO_3 structures

The discovery of new cathode material is key to realising safe and efficient electrochemical energy storage. The reaction of transition metal structures with carbonates have the potential to provide high capacity. Here we show the potential of mixing the transition metal carbonates together. We show that mixing Mn, Ni and Co with CO_3 can produce a better class of cathode materials for lithium ion batteries, hence we utilise cluster expansion to mix different phases.

4.1. Cluster Expansion

Cluster expansion (CE) is a power series expansion of the partition function which was proposed by Mayer and is often applied in models of material calculations [78]. Cluster expansion allows the extraction of atom-atom interactions from a set of first principles and small unit cell calculations. To model real materials in CE requires accurate energy values for systems with millions of atoms and also require quick sampling of millions for such systems in ensembles to acquire good statistics. Cluster expansion method is an effective tool to connect quantum mechanics with large scale atomistic simulation [79].

Modern DFT methods are able to calculate material properties with reasonable to high precision (depending on the quality of the approximations to the exchange and correlation effects). Standard DFT applications are, however restricted to unit cells of a few hundreds of atoms. If one wants to model an alloy with varying atomic concentrations and crystal structures, a huge number of very large supercells would be needed. Such a procedure is of course, not

feasible. A successful strategy to overcome this limitation is offered by the cluster expansion (CE) [80] in particular when combined with Monte Carlo simulations.

4.2. Basic principles of Cluster Expansion

From an optimised cluster expansion, a set of effective cluster interactions can be extracted and used in large-scale Monte Carlo simulations to explore order-disorder phenomena and phase segregation processes as a function of temperature.

On a basic lattice various atoms, for example of type A and B, are distributed to define structure σ, a periodic configuration of A and B atoms. This configuration is described by the pseudo spin operator σq =$\pm$1, which has the value +1 if an atom A sits on site q or -1 if that atom is B.

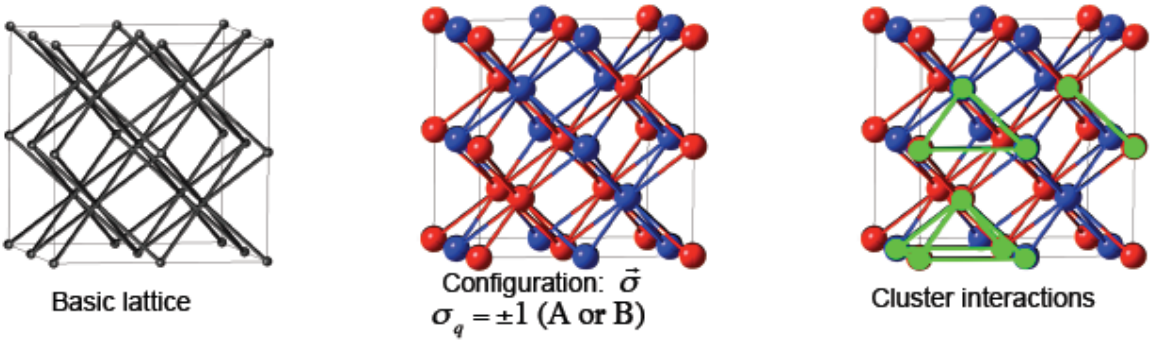

The energy (σ) associated with structure σ can be described by an expansion of cluster interactions and their respective interaction energies J by means of equation

$$E(\vec{\sigma}) = J_0 + J_1 \sum_i \sigma_i + \sum_{i>j} J_{ij}\sigma_i\sigma_j + \sum_{i>j>k} J_{ijk}\sigma_i\sigma_j\sigma_k + \cdots \quad (4\text{-}1)$$

In equation (4-1), J_0 describes a constant configuration independent contribution. The second term is concentration dependent and is the sum over all N sites of structure σ with onsite energy J_1 times the pseudo spin operator σ at each site i. Further terms describe the cluster interactions between multiple sites, for example two-body interactions J_{ij} or three-body interaction J_{ijk}. They

contain spin products $\sigma_i\sigma_j\ldots$ over all f vertices of a cluster times its effective cluster interaction energy $J_{ij\ldots}$ summed up over all the possible ways that the cluster can be placed on the lattice of structure σ. In other words, the energy (σ) of structure is broken down into clusters with their associated effective interaction energies. The core issue of cluster expansion is to identify a universal set of interactions J best-suited to describe a given model. To accomplish this, it is useful to reformulate above equation into the more compact form.

$$E(\vec{\sigma}) = \sum_{C\epsilon\vec{C}} J_C \, \Pi_C(\vec{\sigma}) \tag{4-2}$$

The cluster expansion equation sums up the product of cluster C's interaction energy J_{C} with its correlation function,

$$\Pi_C(\vec{\sigma}) = N^{-1} \sum_{i=1}^{N} \sum_{k\in C} \prod_{v\epsilon\vec{f}} \sigma_v \tag{4-3}$$

The sum over all the possible ways that a cluster C with $\vec{f}$ vertices can be placed on the N sites of the structure. In the correlation function the spin product $\sigma_1 \ldots$ goes over all f vertices of the cluster. Only symmetry in-equivalent clusters are now considered and clusters included in an expansion can be collected by the vector $C = \{C_1,\ldots, C_{\mathrm{n}}\}$.

4.3. UNCLE code

All the cluster expansion calculations for the study were performed by the program named the Universal Cluster Expansion (UNCLE) which was developed by the group of S. Muller [81]. The code is applicable to as many systems as possible, it requires little user input and it also contain efficient tools for the use of ECI's such as kinetic and thermodynamic Monte Carlo simulation. UNCLE code is also able to perform a complete cluster expansion fit using a genetic algorithm to predict the ground states of systems containing up to three and more elements. For deriving results for temperatures T=0, Monte Carlo simulations are implemented. The working scheme used by the cluster expansion for finding input structure is displayed in

figure 4.5. The crucial task of a converged CE is to guarantee that chosen interactive energy and figures are not biased by the training set. To avoid wrong interpretation of the whole system by choosing wrong input, UNCLE uses the chosen figure set to fit the energy of other structures. New structures can now be designed and if they lie energetically below the existing ground state line they are recalculated by DFT, providing a new set of input structures.

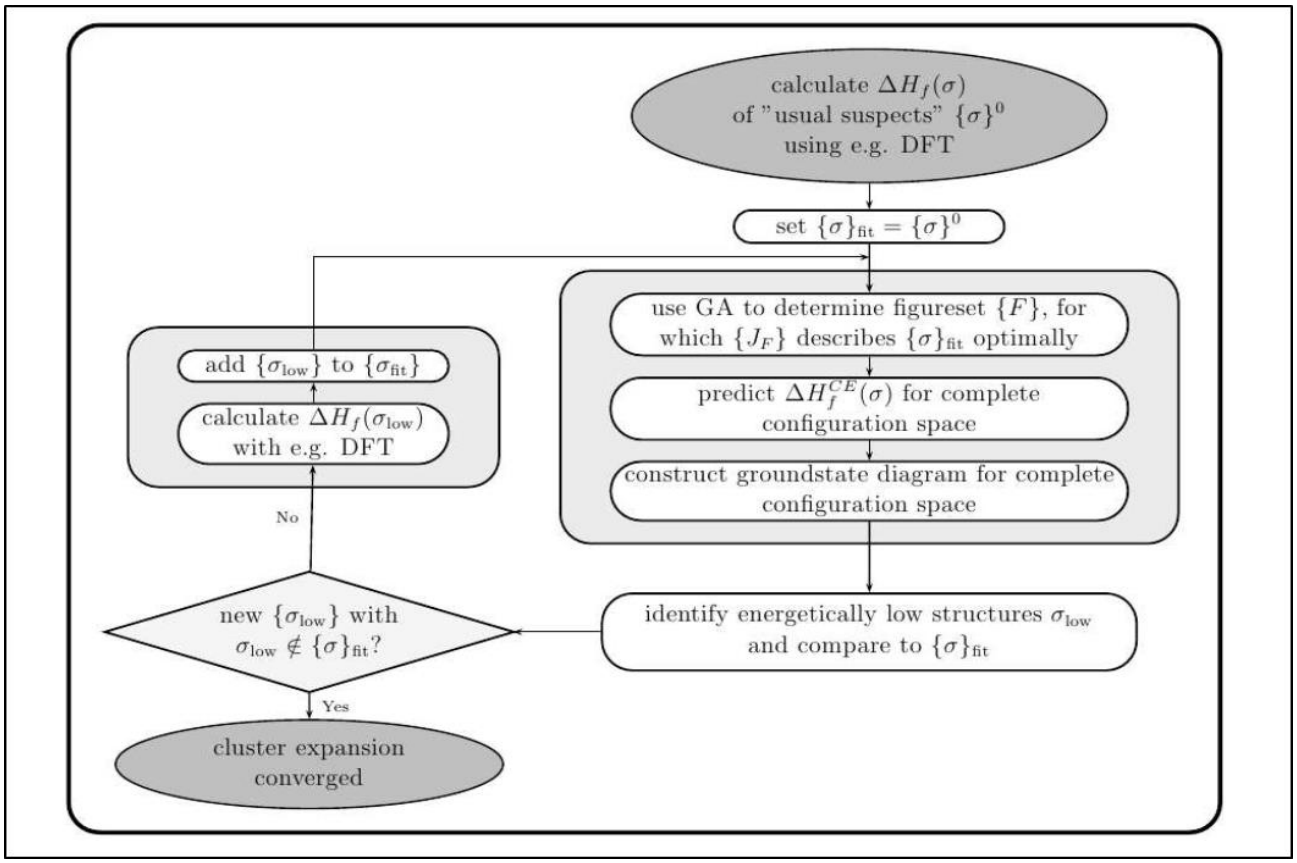

Figure 4.1. illustration of the self-consistent working plan used by UNCLE to choose the input structures of the cluster-expansion [82].

4.4. Genetic Algorithm

A minimization using genetic algorithm was first used for the CE by Hart *et al*. [83]. In this approach the figure list is represented as a binary string. A figure used is marked by the value 1, otherwise the value is 0. Furthermore, the interaction energies are also represented as a binary string. The combination of both binary strings, including figures used and their interaction

energies, is now the genetic 'DNA' of a solution, who's fitness is described by the CVS. A higher CVS compared to other solutions means, that this solution has a lower fitness.

Now, a 'population' of n_{pop} different solutions is created, in which the fitness of every individual solution is calculated. Of those n_{pop} individuals only the fittest n_{fit} ($0 < n_{fit} < n_{pop}$) individuals are selected to survive to the next iteration process. The other $n_{pop} - n_{fit}$ solutions are replaced by 'descendants' of the surviving fittest 'parent' solutions. Their 'DNA' is created by two different processes as shown in figure 4.6.

• In crossover, the 'DNA' of the 'offspring' is created by mixing the 'DNA' of two randomly selected 'parent' solution. Thereby the 'DNA' of one 'parent' solution is used up to the crossover point. After that point the 'DNA' of the second 'parent' is used.

• In mutation, a random binary bit of the 'DNA' string is flipped from one state to the other, i.e. $1 \Rightarrow 0$ or $0 \Rightarrow 1$.

Note that one may replace all surviving 'parent' solutions with the 'children', for as long as only the fittest 'parent' solutions are used to create them.

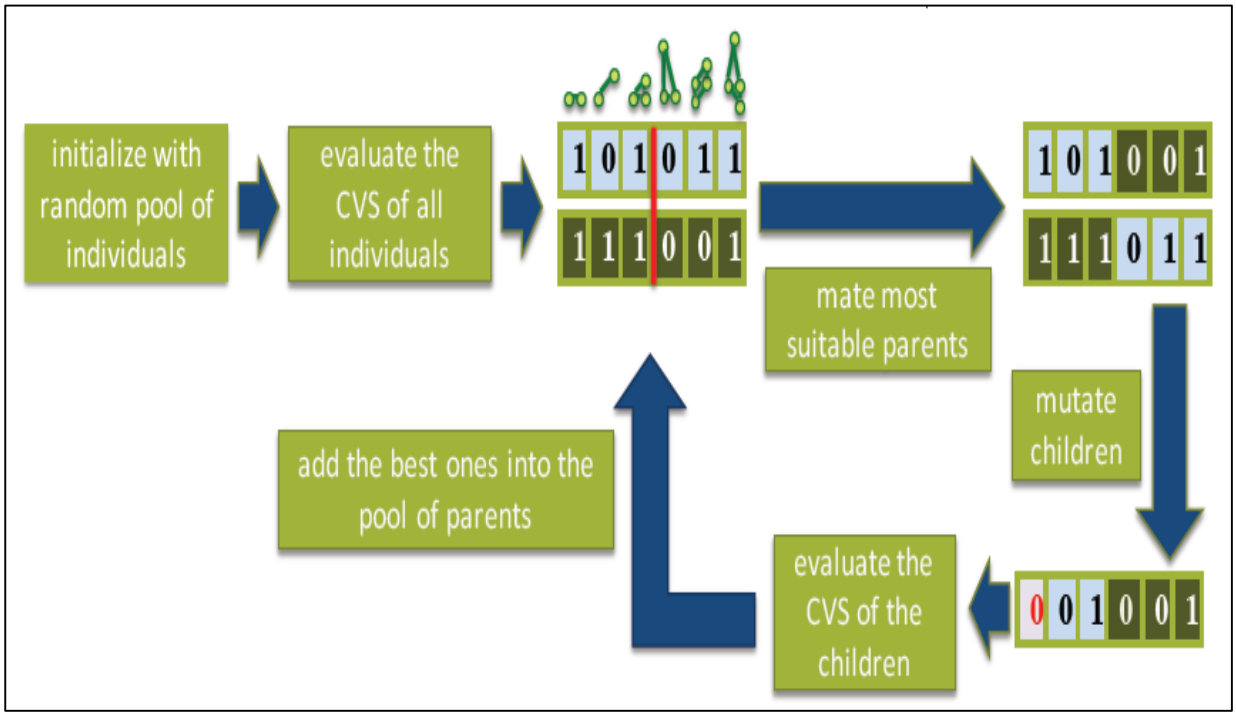

Figure 4.2. Illustration of the genetic algorithm [83].

4.5. Running cluster expansion

After the genetic algorithm has converged, a set of figures is chosen to describe the system best. This set predicted all the DFT derived ground state energies of the starting input set and resulted in the lowest SC_V. Structures, which were not members of the input set of the GA run, should now be predicted sufficiently correct. Now, the ECIs as derived from the fitting are taken to describe all possible structures of the system on the given parent lattice. If the enthalpy of formation of one of these structures is below the ground state line as defined by the DFT input data, this structure is included in an enlarged input set. As a consequence, its formation enthalpy is calculated by DFT and added it to the list of input structures. With this enlarged input set, a new GA is done. This procedure is repeated until no new ground states are predicted by the CE. As a result, the stable structures of the system are obtained and the final ground state line.

4.5.1. Miscible Constituents

If a model has miscible constituents, the structures with energies close to the ground states have the lowest ΔH_f at a given concentration, are the most important ones, and the cluster expansion should be most accurate for those. To accomplish this, those structures predicted by the cluster expansion to be more favourable (with a lowerΔH_f) are not yet part of the training set but are added to the training set. This is done iteratively until no new structures are predicted by cluster expansion to be more favourable than those already included in the training set. At this point, the cluster expansion has converged and from all structures considered by the cluster expansion the thermodynamically stable ones have been identified.

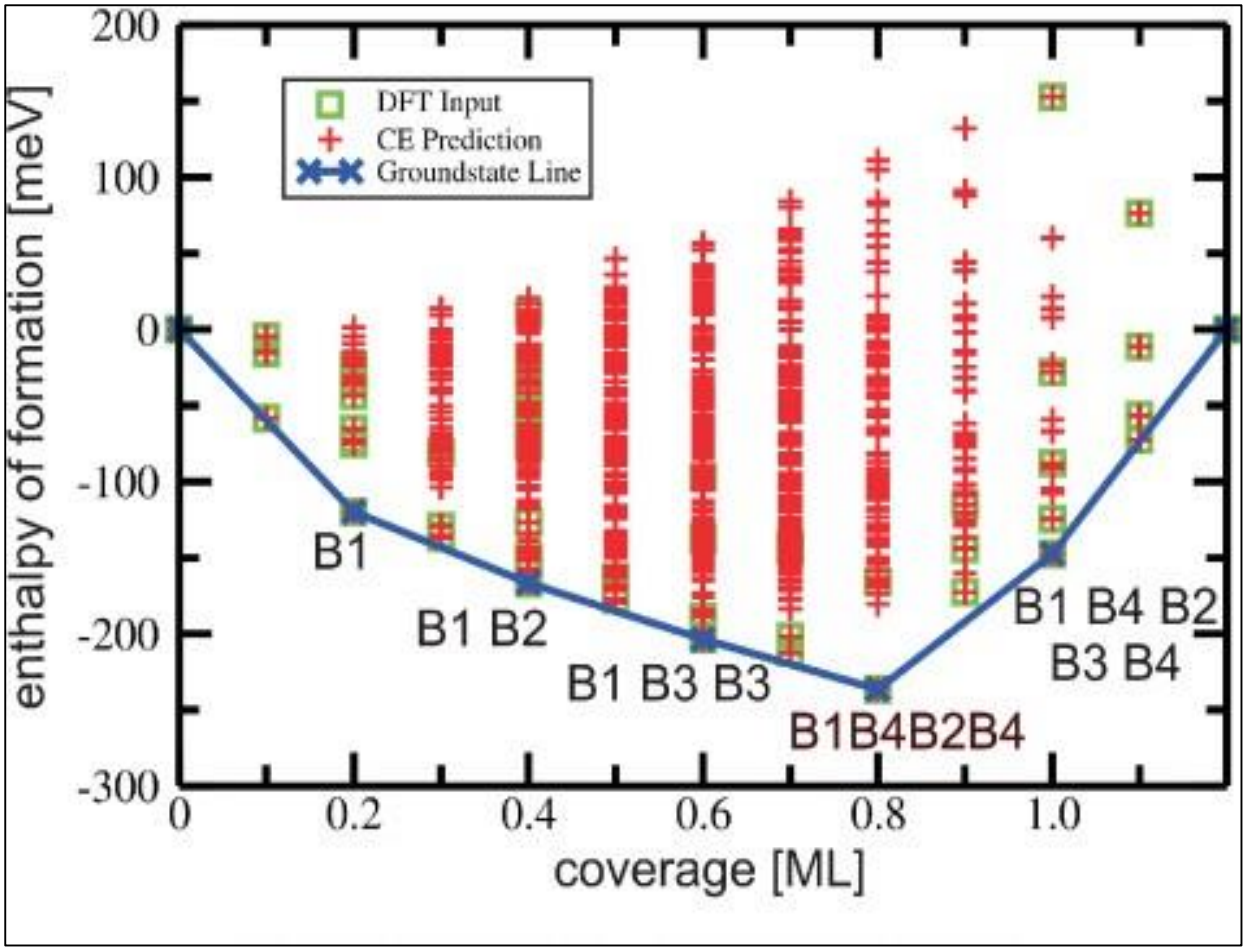

Figure 4.3. Binary ground state diagram illustrating both miscible constituent and miscibility gap [82].

4.5.2. Miscibility Gap

If the model is a phase separating, no stable ordered structures exist apart from the two pure phases and all structures are of equal importance to the cluster expansion. Therefore, the selection process of structures to be added to the training set has to improve the quality of the cluster expansion for all structures considered, irrespective of their formation energies ΔH_f.

To determine how good (or bad) the energies of the structures are predicted by the cluster expansion, the stochastic nature of the genetic algorithm is used. Multiple cluster expansions are performed using an identical training set. The energy of all considered structures are then predicted by these multiple J's and a standard deviation of the predicted energies is evaluated.

Structures with the highest standard deviation are those whose description by the cluster expansion is the worst. Therefore, these are added iteratively to the training set.

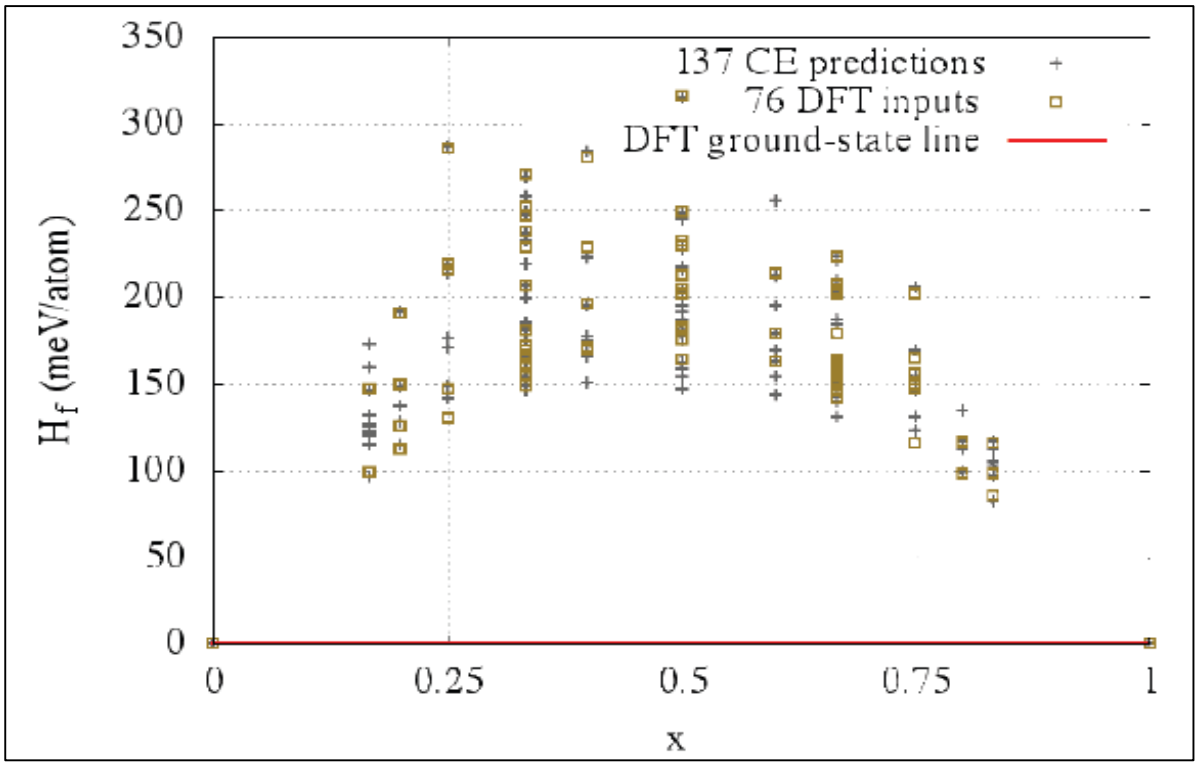

Figure 4.4. Binary ground state diagram illustrating miscibility gap [84].

4.6. Monte Carlo simulations

Monte Carlo methods are used to identify the ordered to disordered transition temperatures. The code performs simulations either within the canonical or grand canonical ensembles. In Monte Carlo simulations, the calculation of energy changes due to the change in energy occupation that can be computed efficiently. Monte Carlo simulation can be used to tackle a range of problems in every field such as finance, engineering and science. In finance, Monte Carlo simulation is used to estimate the probability of cost overrun in large projects. Cluster expansion needs effective interaction energies (ECI), which in the present case were derived from standard DFT calculations. However, DFT total energies are only valid for temperature T=0K, so in order to include temperature effects in the system, one might have to think about configurational entropies.

4.6.1 Grandcanonial Ensemble

The grand canonical ensemble is also called the µV T ensemble. It describes systems in contact with a thermostat at temperature T and a particle reservoir that maintains the chemical potential µ. The chemical potential µ is a thermodynamic which controls the propagation of the atoms in and out of the box. If the chemical potential of one atom type in the system is raised, then the number of atoms of this type will be decreased. The reason for that is if one atom is removed from the system and another one is added then the chemical potential changes by $\Delta\mu = \mu_A - \mu_B$ with μ_i being the chemical potential for atomic species. The system not only exchanges heat with the thermostat, it also exchanges particles with the reservoir while the volume V remain fixed and the number of particles N and energy E fluctuate at thermal equilibrium [85].

4.6.2 Canonical Ensemble

In a canonical ensemble the conserved quantity is the concentration of each atom type in the simulation box. In each step the position of two randomly chosen atoms is exchanged. The random walk through phase space is continued until a chosen number of steps is done or the change in the energy of the system is below a given numerical limit. Doing so, the energy of the composition in box changes and the transition rate can be written as;

$$P^*_{\sigma\sigma'} = \begin{cases} 1 & \text{if } \epsilon < e^{-(E(\sigma')-E(\sigma))/kT} \\ 0 & \text{if } \epsilon > e^{-(E(\sigma')-E(\sigma))/kT} \end{cases} \quad (4\text{-}4)$$

4.7. Results and Discussion

4.7.1 Search for the Ground States

In computational material science, we utilise cluster expansion technique to predict the ordered or disordered superstructures. Cluster expansion plays a conjunction role in combination and it could be combined with first-principles calculations or be used independently. In this study, we combined first-principles calculations with cluster expansion to identify the stable configurations on MCO_3 structures. Table 4.1 display the ground state enthalpy of formations for $MnNiCO_3$ structure as predicted by the DFT and CE. DFT was unable to predict the ground state energies due to the larger cells of the system. However, cluster expansion was used as an alternate method since it does not limit the number of atoms used per each system. The ground-state search of binary compounds by total-energy calculations and diagrammatic approaches suffers largely from the need that the small group of crystallographic configurations considered must include the stable one.

Table 4.1. Listing stable structures therefore only contains pure phases.

Iteration	no. of struc.	no. of new struc.	CVS [meV/pos.]	% struc. with SD below 5 meV	new structures
0	0	2	-	-	ce1 ce3
0	0	6	-	-	ce29581 ce70758 ce61758 ce9190 ce1 ce3
1	6	4	4.5	-	ce21259 ce1 ce1006 ce65
2	9	4	0.025	-	ce1847 ce463 ce445 ce15592
3	13	4	0.0012	-	ce94029 ce14613 ce162 ce2089
4	17	4	0.0013	-	ce11239 ce2537 ce5783 ce379
5	21	4	0.027	-	ce8 ce692 ce6105 ce15683
6	25	4	4.9	-	ce521 ce7467 ce15295 ce5773
7	29	4	10	-	ce5490 ce519 ce605 ce47453
8	33	4	13	-	ce5775 ce5842 ce17495 ce18
9	37	4	11	-	ce7369 ce43586 ce15351 ce503
10	41	4	12	-	ce770 ce13980 ce6467 ce6459
11	45	4	12	-	ce1839 ce414 ce40803 ce61909
12	49	4	8.5	-	ce22 ce7898 ce713 ce5783
13	52	4	13	-	ce1018 ce1 ce332 ce6487
14	55	4	12	-	ce35454 ce498 ce7825 ce4194
15	59	4	9.5	-	ce91600 ce859 ce563 ce47215
16	63	4	9.4	-	ce7799 ce342 ce5775 ce69154
17	66	4	9.4	-	ce715 ce14415 ce572 ce645
18	70	4	10	-	ce1013 ce1872 ce15351 ce47335
19	73	4	9.7	-	ce1198 ce15500 ce29317 ce9880
20	77	0	9.1	-	ce1198 ce15500 ce29317 ce9880

For this study, our main focus is mixing transition metal carbonate structures to determine the stable phase diagrams after the convergence. Figure 4.5, 4.7 and 4.8 show binary phase diagrams of $MnNiCO_3$, $CoMnCO_3$ and $CoNiCO_3$. We note that all the phases predicted are in the negative energy of formations (miscible constituent) indicating thermodynamic stability. However, the most stable structures are those appearing on the DFT ground state line. Miscible constituent's behaviour indicate that structures are ordered and thermodynamically stable. Similarly to $MnNiCO_3$, $CoMnCO_3$ and $CoNiCO_3$, the binary phase diagram for $NiMnCO_3$ as shown in Figure 4.6 indicate a miscible constituent behaviour because all the predicted structures are in the negative energy of formations. However, we also note that below the ground state line appears other predicted phases or structures which indicate that the material did not fully converge. Moreover, the green squares shown in phase diagram represent structures which are most favourable within a bcc-type lattice phases, which were predicted as ground state structures in the CE run and structures on the ground state line are also thermodynamically stable. The maximal size of the unit cells for the CE predictions were adjusted during the fitting procedure and the largest unit cell contained 77 atoms.

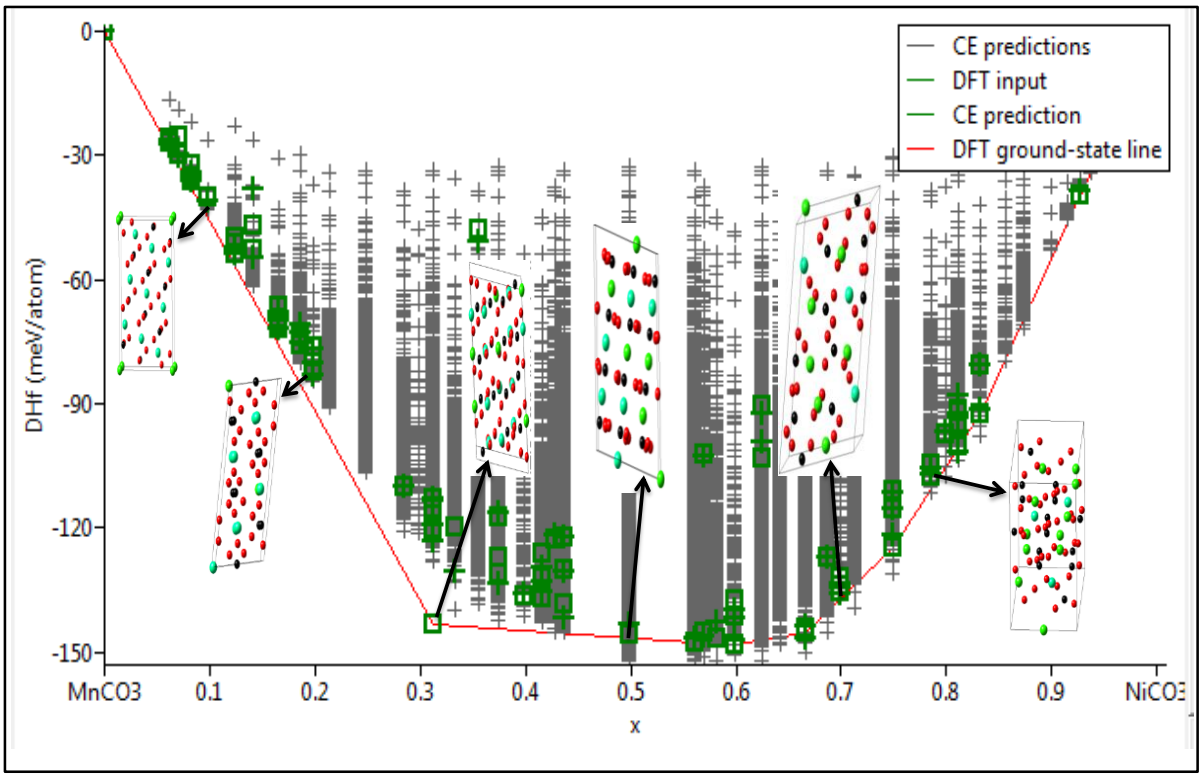

Figure 4. 5. Binary phase diagram of mixed $MnNiCO_3$

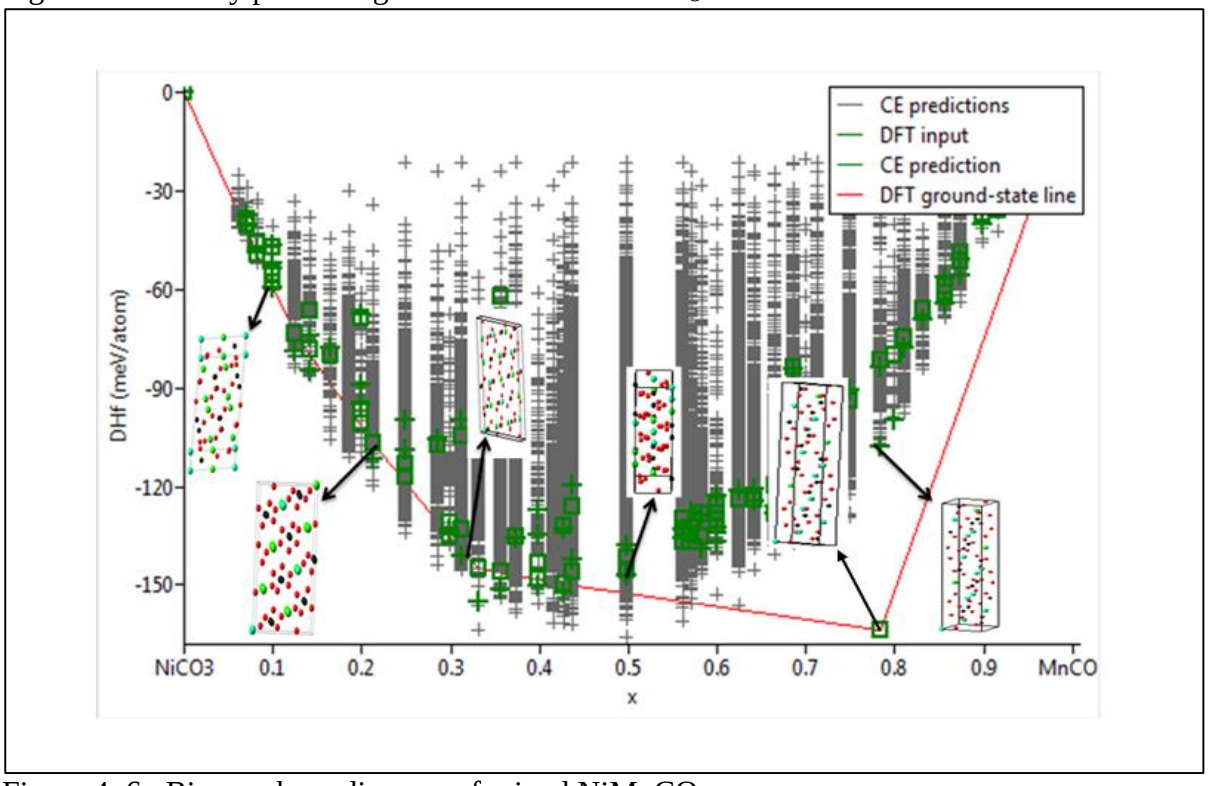

Figure 4. 6. Binary phase diagram of mixed $NiMnCO_3$

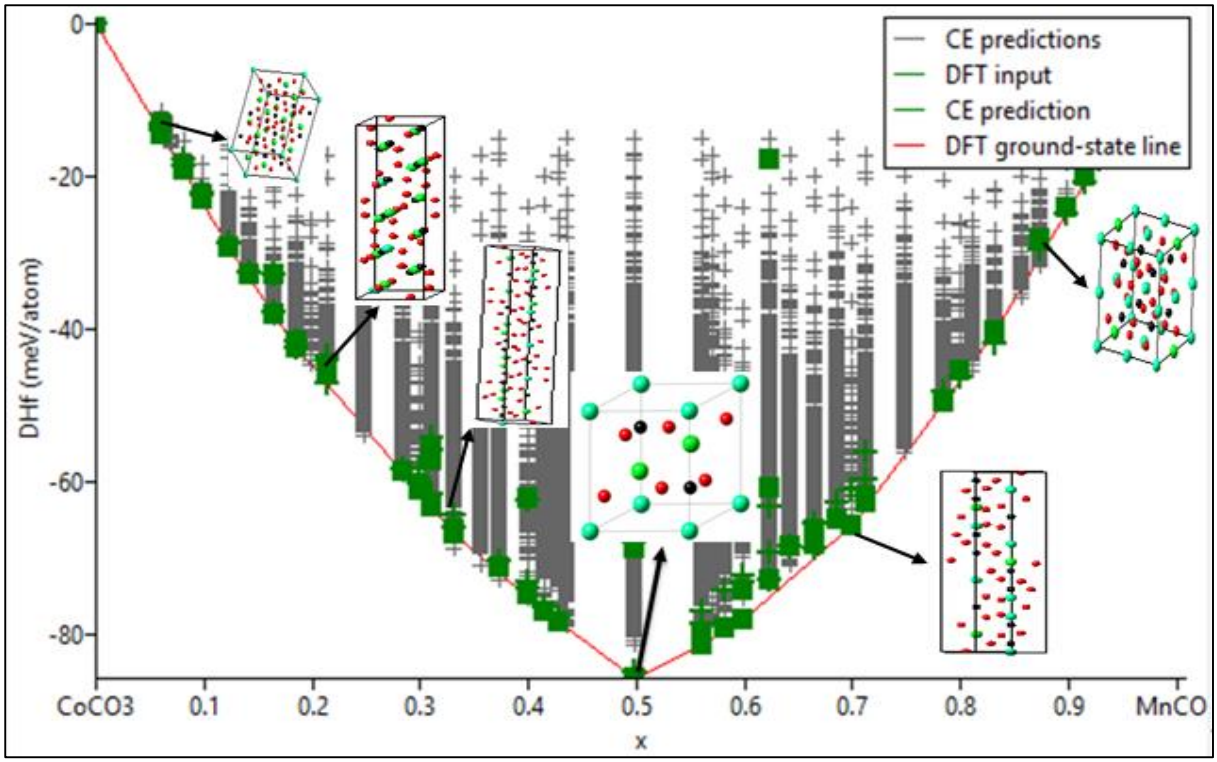

Figure 4. 7. Binary phase diagram of mixed $CoMnCO_3$

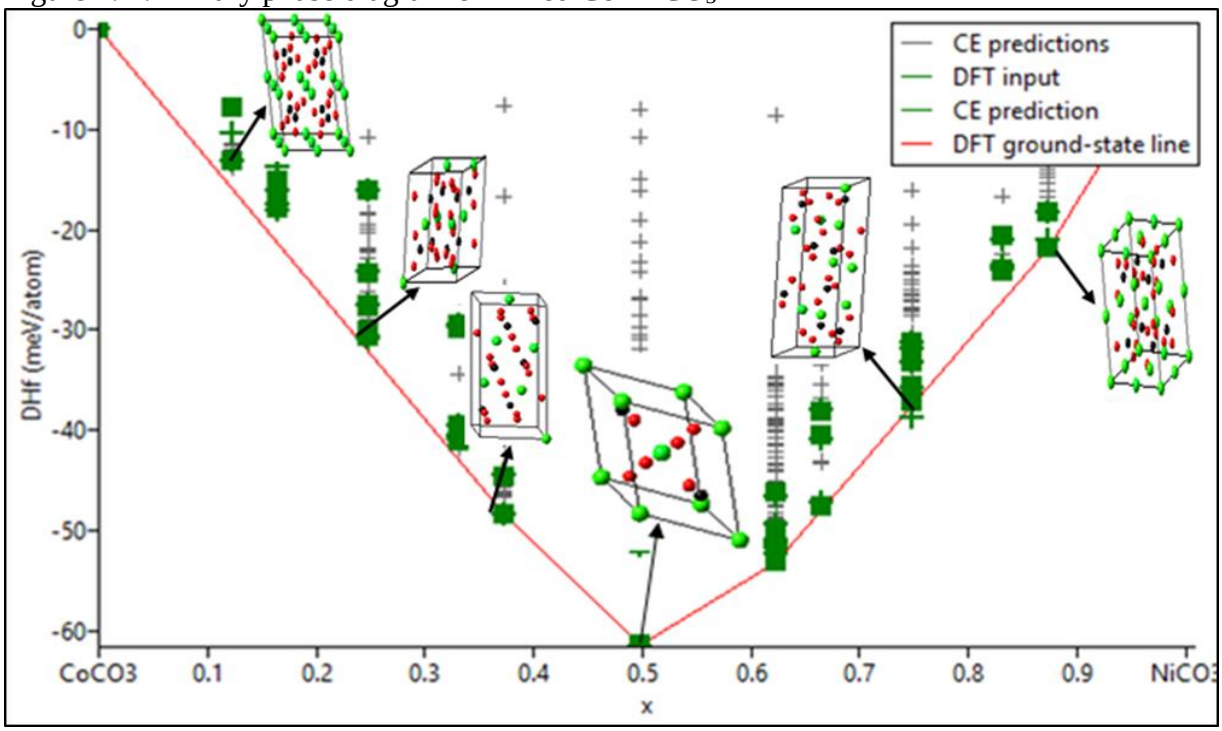

Figure 4. 8. Binary phase diagram of mixed $CoNiCO_3$

4.8. Elastic constants for most stable structures from cluster expansion

The generated phases from cluster expansion were optimised and stable structures were utilised to calculate the elastic constants, density of states and phonon dispersion curves. Elastic constants provide significant information on the mechanical properties of materials and their

structural stability [86]. The elastic constants for stable structures obtained from CE were found to be triclinic crystal systems. Triclinic materials are categorized as anisotropic elastic materials with no existence of a symmetry plane and are said to have 21 independent elastic constants. The calculated independent elastic constants for $MnNiCO_3$ and $NiMnCO_3$ at ambient pressure are shown in Table 4.1 and 4.2 respectively. The negative eigenvalues indicate that the structure is unstable. We further calculated the density of states for most stable structures from the binary phase diagram to determine if materials are metals, insulators or semi-conductors and we found that the structures are semi-conductors since there is a band gap observed at the Fermi level. The partial DOS diagram shows elements which are responsible for the energy band gap at the Fermi level.

Table 4. 2. Elastic constants (GPa) for $NiMnCO_3$ at 50%

C_{ij}	Elastic constants 50% $NiMnCO_3$
C_{11}	138.59
C_{12}	64.25
C_{13}	76.80
C_{14}	1.88
C_{15}	1.38
C_{16}	4.16
C_{22}	231.27
C_{23}	74.22
C_{24}	0.47
C_{25}	12.00
C_{26}	8.21
C_{33}	229.55
C_{34}	-0.92
C_{35}	-5.93
C_{36}	21.60
C_{44}	64.48
C_{45}	18.56
C_{46}	0.93
C_{55}	55.74
C_{56}	-2.35
C_{66}	42.39

Table 4. 3. Elastic constants (GPa) for $NiMnCO_3$ at 30%

C_{ij}	Elastic constants 30% $NiMnCO_3$
C_{11}	194.70
C_{12}	69.530
C_{13}	71.520
C_{14}	-5.08
C_{15}	-22.97
C_{16}	20.70
C_{22}	167.02
C_{23}	61.99
C_{24}	17.86
C_{25}	11.56
C_{26}	21.63
C_{33}	226.70
C_{34}	-2.02
C_{35}	-4.35
C_{36}	11.24
C_{44}	49.64
C_{45}	12.06
C_{46}	6.15
C_{55}	51.72
C_{56}	-1.00
C_{66}	49.53

4.9. Electronic properties

In order to gain knowledge on the electronic conductivity of MCO_3 structures, we have calculated their densities of states (DOS). We note that the total and partial DOS are separated, forming a band gap near the Fermi level (E_F). The concepts of Fermi level and band gaps are necessary to understand the electronic conductivity of materials. Figure 4.9 display the total and partial density of states for $MnNiCO_3$ (a), $NiMnCO_3$ (b), $CoMnCO_3$ (c) and $CoNiCO_3$ (d). We note the presence of energy band gap near the fermi level for all the structures which suggest a semi-conductor or insulator behaviour. The system is said to be an insulator if the energy band gap is more than 3eV and semiconductor if the band gap is less than 3eV. The total DOS peak of $MnNiCO_3$ and $NiMnCO_3$ located at this energy range (-10eV to 0eV) reflects the strong hybridisation between Mn *d*-states and Ni *d*-states. Similarly, for $CoMnCO_3$ and

$CoNiCO_3$, the total DOS peak located at (-10eV to 0eV) reflects the hybridisation of Co, Mn and Ni *d*-states.

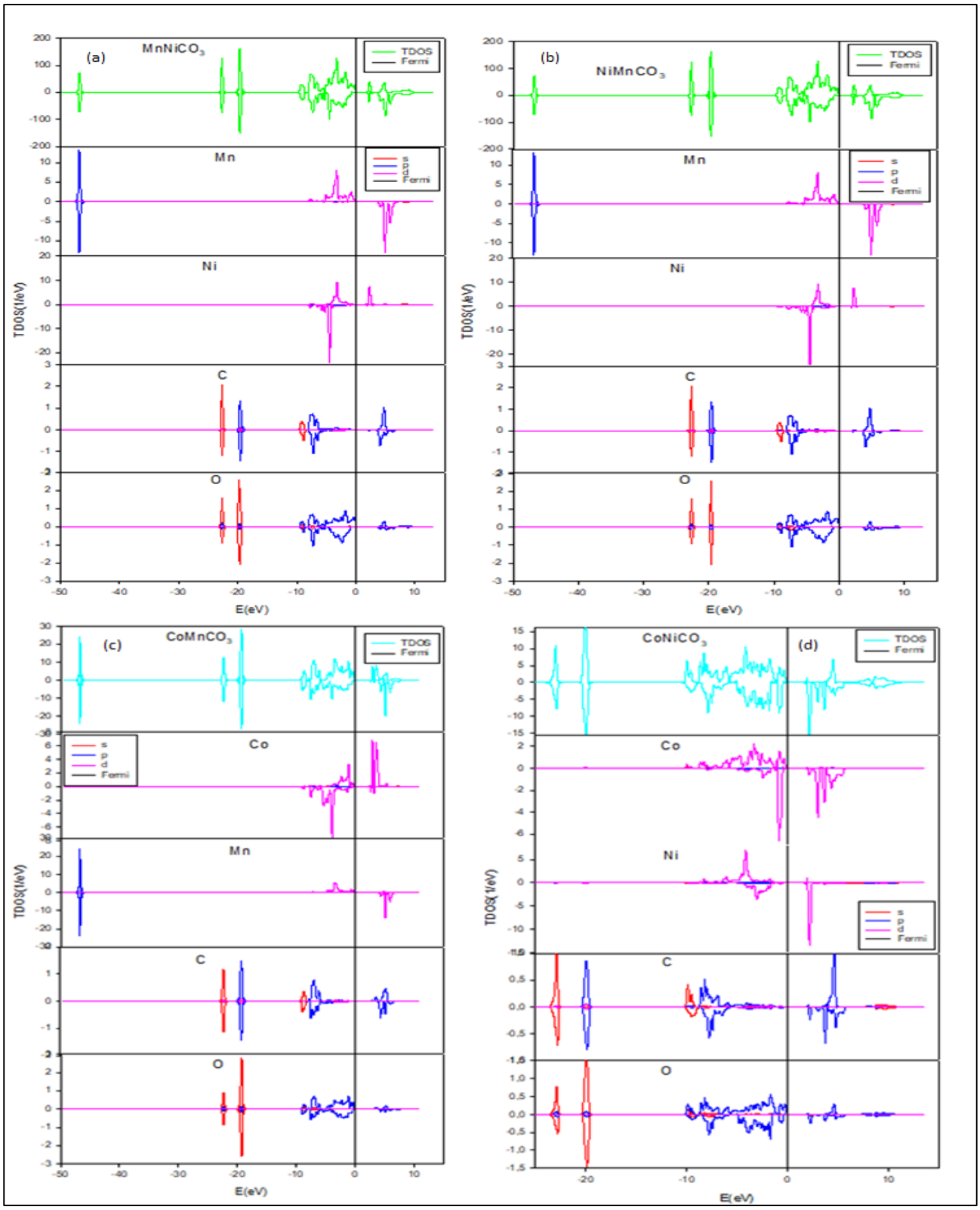

Figure 4. 9. Total and Partial DOS for (a) $MnNiCO_3$, (b) $NiMnCO_3$, (c) $CoMnCO_3$ (d) $CoNiCO_3$.

CHAPTER 5

5.1. Conclusions

First principle DFT+U calculations were employed to investigate the structural, thermodynamic, electronic, elastic and vibrational properties of the transition metal carbonates (MCO_3) at 0K to mimic their stability. Our DFT+U calculated lattice parameters were found to be in good agreement with the available experimental data to within 10% validating the approach employed. To investigate thermodynamic stability of MCO_3, heats of formations were calculated. All heats of formation values were predicted to be very low and negative, suggesting that MCO_3 structures are formidable experimentally. Moreover, the heats of formations were found to be increasing with the transition metals, suggesting a decrease in energetic stability. The stability trend was observed as follows: $CaCO_3 > MnCO_3 > FeCO_3 > NiCO_3 > CoCO_3$.

The analysis of electronic properties was done by calculating band structures and density of states (DOS). $CaCO_3$ and $MnCO_3$ showed insulator behaviour characteristic while $NiCO_3$ and $CoCO_3$ were predicted to be semiconductors and $FeCO_3$ metallic. The partial densities of states showed that the states around Fermi level are predominantly from the d-orbital of the transition metals. The calculated elastic constants suggested mechanical stability for $CaCO_3$, $MnCO_3$, $CoCO_3$ and $NiCO_3$ structures, since they satisfied the necessary Born stability criterion for trigonal crystals. On the other hand, $FeCO_3$ was predicted to be mechanically unstable, since the stability conditions $(C_{44} + C_{12})C_{33} - 2C_{13}^2 > 0$ and $(C_{11} + C_{12})C_{44} - 2C_{14}^2 > 0$ were not satisfied. The macroscopic Bulk and Young's moduli were found to be high and positive suggesting hardness and stiffness. Moreover, the Pugh's ratio (B/G) for ductility and brittleness showed that $CaCO_3$, $FeCO_3$ and $NiCO_3$ are brittle since B/G is less than 1.75 while $MnCO_3$ and $CoCO_3$ were found to be ductile (B/G > 1.75). The phonon dispersion curves for $CaCO_3$,

$MnCO_3$, $NiCO_3$ and $CoCO_3$ structures showed no availability of soft modes along the high symmetry zone suggesting vibrational stability. On the other hand, the phonon dispersion curve for $FeCO_3$ showed the presence of soft modes (negative frequencies) along high symmetry directions in the Brillouin zone which indicates vibrational instability of the material. Cluster expansion methods were also utilised in the study to determine stable phases from binary phase diagrams. We note that all the predicted phases of $MnNiCO_3$, $CoMnCO_3$ and $CoNiCO_3$ are displayed in the negative energy of formations, suggesting thermodynamic stability. However, the most stable structures are the once appearing on the DFT ground state line. Moreover, cluster expansion methods were employed to generate 77 new stable phases from a binary phase diagram. The new phases generated depict a miscible constituents whereby structures with energies close to the ground states have the lowest ΔH_f at a given concentration. Furthermore, the mixed systems $Ni_{1-x}Mn_xCO_3$ exist at Mn-rich side, while $Co_{1-x}Ni_xCO_3$ and $Co_{1-x}Mn_xCO_3$ are favourable at equiatomic (50:50) concentrations.

5.2. Recommendations and future work

At present, the most successful rechargeable battery is the Li-ion battery due to the small size, high energy density and low reduction potential of Li [87]. Computational materials science has become an increasingly important tool to study these batteries, in particular cathode materials [88]. In this study, First principle calculations have been used to study the key properties such as structural stability, electronic structure etc. Temperature is known to have a significant impact on the performance, safety and cycle lifetime of lithium-ion batteries. To explore properties at different temperatures of the binary and ternary systems of precursor materials, molecular dynamics and Monte Carlo simulations could be employed. The possible fitting and derivation of interatomic potential models for binary carbonate precursors using GULP code and Force Field Optimizer codes. A further study could also be required on diffusivity of binary and ternary phases using MedeA-UNCLE code.

5.3. Papers presented at conferences

1. M.T Morukuladi. N.L Lethole, M.C Masedi, and P.E. Ngoepe "First-Principle Studies of MCO_3 (M: Ca, Mn, Fe, Co, Ni) Precursor Materials for Lithium Ion Batteries", Faculty of Science and Agriculture Research Day, Fusion Boutique Hotel, Polokwane, September 2018.
2. M.T Morukuladi. N.L Lethole, M.C Masedi, and P.E. Ngoepe, "Computational Modelling of Transition Metal Carbonate Precursor Materials for Li-ion batteries", Centre for High Performance and Computing (CHPC), Century city conference hall, Cape Town, December 2018.
3. M.T Morukuladi. N.L Lethole, N.N Ngoepe, M.C Masedi, and P.E. Ngoepe, "Structural, thermodynamic, electronic and mechanical properties of MCO_3 (M: Ca, Mn, Fe, Co, Ni) precursor materials for Li-ion batteries" South African Institute of Physics (SAIP), The Ranch Hotel, Polokwane, July 2019.
4. M.T Morukuladi. N.L Lethole, N.N Ngoepe, M.C Masedi, and P.E. Ngoepe, "Density Functional Theory Study for Computational Modelling of Transition Metal Carbonate Precursors for Lithium Ion Batteries" Faculty of Science and Agriculture Research Day, The Ranch Hotel, Polokwane, September 2019.

5.4. References

[1] V. Etacheri, R. Marom, R. Elazari, G. Salitra and D. Aurbach, "Challenges in the Development of Advanced Li-ion Batteries: A Review," *Energy Environmental Science,* vol. 4, pp. 3243-3262, 2011.

[2] D. Deng, "Li-ion batteries: basics, progress, and challenges," *Energy Science & Engineering,* vol. 3, pp. 230-300, 2015.

[3] B. Dunn, H. Kamath and J.M. Tarascon, "Electrical Energy Storage for the Grid: A Battery of Choices," *Science,* vol. 334, pp. 928-935, 2011.

[4] N. Nitta, F. Wu, J.T. Lee and G. Yushin, "Li-ion Battery Materials: Present and Future," *Materialstoday,* vol. 18, pp. 252-264, 2015.

[5] K.C. Jiang, S. Xin, J.S. Lee, J. Kim, X.L. Xiao and Y.G. Guo, “Improved Kinetics of LiNi1/3Mn1/3Co1/3O2 Cathode Material through Reduced Graphene Oxide Networks,” *Physical Chemistry Chemical Physics,* vol. 14, pp. 2934-2939, 2012.

[6] M. Yoshio, R.J. Brodd and A. Kozawa, “Lithium Ion Batteries,” *Springer,* vol. 46, pp. 03873-04464, 2009.

[7] C.M. Julien, A. Mauger, K. Zaghib and H. Groult, “Comparative Issues of Cathode Materials for Li-Ion Batteries,” *Inorganics,* vol. 2, pp. 132-154, 2014.

[8] J.J. Liu, J.Wang, Y.G. Xia, X.F. Zhou, Y. Saixi and Z.P. Liu, “Synthesis and Electrochemical Performance of Li1+xNi0.5Mn0.3Co0.2O2+delta (0 <= x <= 0.15) Cathode Materials for Lithium-ion Batteries,” *Materials Research Bulletin,* vol. 47, pp. 807-812, 2012.

[9] P. Mohan and G.P. Kalaignan, “Structure and Electrochemical Performance of LiV x Mn2 − x O4 (0 ≤ x ≤ 0.20) Cathode Materials for Rechargeable Lithium ion Batteries,” *Ionics,* vol. 19, pp. 895-900, 2014.

[10] K.S. Lee, S.T. Myung, J.S. Moon and Y.K. Sun, “Particle Size Effect of Li[Ni0.5Mn0.5]O2 Prepared by Co-Precipitation,” *Electrochimica Acta,* vol. 53, pp. 6033-6037, 2008.

[11] G. Koenig, G. Zhou and K.Amine, “Growth Mechanism of Ni0.3Mn0.7CO3 Precursor for High Capacity Li-ion,” *Journal of Materials Chemistry,* vol. 21, pp. 9290-9300, 2011.

[12] T.H. Cho, S.M. Park, M. Yoshio, T. Hirai and Y. Hideshima, “Effect of Synthesis Condition on the Structural and Electrochemical Properties of Li[Ni 1/3Mn 1/3Co 1/3]O2 Prepared by Carbonate Co-Precipitation Method,” *Journal of Power Sources,* vol. 142, pp. 306-312, 2005.

[13] R.C. Longo, K.C. Santosh, F. Kong and M.S. Park, “Phase Stability of Li-Mn-O Oxides as Cathode Materials for Li-ion Batteries: Insights from ab initio Calculations,” *Physical Chemistry Chemical Physics,* vol. 16, pp. 11233-11242, 2014.

[14] A. Simon and T. Redferm, “Structural Variations in Carbonates,” *Reviews in Mineralogy and Geochemistry ,* vol. 41, pp. 289-308, 2000.

[15] R. Chaohui, X. Guo, M. Li, X. Sun, X. Lian, H. Wang, X. Gao, B. Niu and W. Li, “In Vitro Preparation and Characterization of Amorphous Calcium Carbonate Nanoparticles for Applications in Curcumin Delivery,” *Journal of Materials Science,* vol. 10, pp. 1-11, 2019.

[16] W.L. Bragg, “The Analysis of Crystals by X-ray Spectrometer,” *Proceedings of the Royal Society,* vol. 89, pp. 468-489, 1914.

[17] J. P. R. De Villiers, “Crystal Structure of Aragonite, Strontianite and Witherite,” *The American Mineralogist,* vol. 56, pp. 758-767, 1971.

[18] W. A. Deer, R. A. Howie and J. Zussman, “An Introduction to the Rock-Forming Minerals,” *Mineralogical Society of Great Britain and Ireland,* vol. 5, pp. 539-540, 2013.

[19] W. Kohn and P. Hohenberg, “Inhomogeneous Electron Gas,” *Physical Review,* vol. 136, p. 864–871, 1964.

[20] P. Hohenberg and W. Kohn, “Inhomogeneous electron gas,” *Physical Review,* vol. 136, pp. 871-880, 1964.

[21] L. H. Thomas, “The Calculation of Atomic Fields,” *Mathematical Proceedings of the Cambridge Philosophical Society,* vol. 23, pp. 542-548, 1927.

[22] D.R. Hartree and V.A. Fock, “The Wave Mechanics of an Atom with a Non-Coulomb Central Field. Part I. Theory and Methods,” *Mathematical Proceedings of the Cambridge Philosophical Society,* vol. 24, pp. 89-110, 1928.

[23] J.C. Slater, “A Generalized Self-Consistent Field Method,” *Physical Review,* vol. 81, pp. 385-395, 1951.

[24] D.M. Hanson, E. Harvey, R. Sweeney and T.J. Zielinski, “Quantum States of Atoms and Molecules,” *Chemistry LibreTexts,* vol. 10, pp. 50-80, 2019.

[25] P. W. Ayers, S. Golden and M. Levy, “Generalizations of the Hohenberg-Kohn Theorem: I. Legendre Transform Constructions of Variational Principles for Density Matrices and Electron Distrbution Functions,” *Journal of Chemical Physics,* vol. 124, pp. 054101-054107, 2006.

[26] W. Kohn and L. Sham, “Self-Consistent Equations Including Exchange and Correlation Effects,” *Physical Review Journals Archive,* vol. 140, pp. 1133-1248, 1965.

[27] M. Chakraverty, H.M. Kittur and P.A. Kumar, “First Principle Simulations of Various Magnetic Tunnel Junctions for Applications in Magnetoresitive Random Access Memories,” *IEEE Transactions on Nanotechnology,* vol. 12, pp. 971-985, 2013.

[28] B. J. Alder and D.M. Ceperley, “Ground State of the Electron Gas by a Stochastic Method,” *Physical Review Letters,* vol. 45, p. 566–569, 1980.

[29] K. Horn and M. Scheffler, “In Electronic Structure,” *Handbook of Surface Science,* vol. 2, pp. 1-1058, 2000.

[30] P. J Perdew, “Density-Functional Approximation for the Correlation Energy of the Inhomogeneous Electron Gas,” *Physical Review B,* vol. 34, p. 7406–7809, 1986.

[31] A. D. Becke, “Density-Functional Exchange-Energy Approximation with Correct Asymptotic Behavior,” *Physical Review,* vol. 38, p. 3098–3100, 1988.

[32] Y. Wang and J.P. Perdew, “Accurate and Simple Analytic Representation of the Electron-Gas Correlation Energy,” *Physical Review,* vol. 45, p. 13244–13249, 1992.

[33] J.P. Perdew, K. Burke and M. Ernzerhof, “Generalized Gradient Approximation Made Simple,” *Physical Review Letters,* vol. 77, pp. 3865-3880, 1996.

[34] E. Wimmer and J. Andzelm, “Density Functional Gaussian-type-Orbital Approach to Molecular Geometries, Vibrations and Reaction Energies,” *The journal of Chemical Physics,* vol. 96, pp. 1280-1289, 1992.

[35] M. Meyer and V. Pontikis, “Application of Computer Simulation in Material Science,” *Applied Mechanics and Materials,* vol. 112, pp. 257-321, 1991.

[36] M. L. Cohen and M. T. Yin, “Theory of Lattice-Dynamical Properties of Solids: Application to Si and Ge,” *Physical Review B,* vol. 26, pp. 3259-3270, 1982.

[37] M. Massimi, “Pauli's Exclusion Principle: The Origin and Validation of a Scientific Principle,” *Cambridge,* vol. 5, pp. 437-590, 2016.

[38] D.R. Hamman, M. Schluter and C. Chiang, “Norm Conserving Pseudopotentials,” *Physical Review Letters,* vol. 43, pp. 1494-1499, 1979.

[39] M. Suzuki and I. S. Suzuki, “Lecture Note on Solid State Physics,” *ResearchGate,* pp. 13902-6000, 2006.

[40] D. J. Cohen and M. L. Chadi, “Special Points in the Brillouin Zone,” *Physical Review,* vol. 8, p. 5747–5753, 1973.

[41] H.J. Monkhorst and J.D. Pack, “Special Points for Brillouin-zone Integrations,” *Physical Review,* vol. 13, pp. 5188-5190, 1976.

[42] P. P. Pratapa and P. Suryanarayana, “Restarted Pulay mixing for efficient and robust acceleration of fixed-point iterations,” *Chemical Physics Letters,* vol. 635, pp. 69-74, 2015.

[43] P. E. Blöchi, “Projector Augmented-Wave Method,” *Physical Review,* vol. 50, pp. 17953-17980, 1994.

[44] P.E. Blochl, “ Projector Augmented-Wave Method,” *Physical Review ,* vol. 50, pp. 17953-17979, 1994.

[45] K.Parlinski, “Molecular Dynamics Simulation of Incommensurate Phases,” *Computer Physics Reports,* vol. 8, pp. 153-219, 1988.

[46] M. Zbiri, R. Mittal, S. Rols, Y. Su, Y. Xiao, H. Schober, S.L.Chaplot, M.R. Johnson, T. Chatterji, Y. Inoue, S. Matsuishi, H. Hosono and T.Brueckel, “Magnetic Lattice Dynamics of the Oxygen-free FeAs,” *Journal for Physical Review,* vol. 22, pp. 315-701, 2010.

[47] M.F. Lu, C.P. Zhou, Q.Q. Li, C. Zhang and H.F. Shi, “Effects of B site Doping on Electronic Structures of InNbO4 based on Hybrid Density Functional Calculations,” *Materials Science and Engineering,* vol. 292, pp. 1757-8992, 2017.

[48] I. Harald and H. Luth, “An Introduction to Principles of Materials Science 2nd edition,” *Solid State Physics,* vol. 2, pp. 541-560, 1996.

[49] Q. Li, S. Danilkin, G. Deng, Z. Li, R.L. Withers, Z. Xu and Y. Liu, “Soft Phonon Modes and Diffuse Scattering in relaxor ferroelectrics,” *Journal of Materiomics,* vol. 4, pp. 345-352, 2018.

[50] M.J. Mehl, B.M. Klein and D.A. Papaconstantopoulos, “First Principle Calculation of Elastic Properties of Metals,” *Naval Research Laboratory,* vol. 4, pp. 589-598, 1993.

[51] L.L Boyer and M.J. Mehl, “Getting off the Bain path: Are there any Metastable States of Cubic Elements?,” *Physical Review,* vol. 43, pp. 9498 - 9502, 1991.

[52] P. Saxeb and Y. Le Pagea, “Ab Initio vs Literature Stiffness Values for Ga: A Caveat about Crystal Settings,” *Physica B: Condensed Matter,* vol. 307, pp. 1-308, 2001.

[53] F. Mouhat and F.X. Coudert, “Necessary and Sufficient Elastic Stability Conditions in Various Crystal Systems,” *Physical Review,* vol. 90, pp. 104-224, 2014.

[54] J. Furthmüller and G. Kresse, “Efficient Iterative Schemes for Ab Initio Total-Energy Calculations using a Plane-Wave Basis Set,” *Physical Review,* vol. 54, pp. 11169-12150, 1996.

[55] P.E. Blochl, “Projector Augmented-Wave Method,” *IBM Research Division, Zurich Research Laboratory,* vol. 50, pp. 17953-17979, 1994.

[56] G. Kresse and D. Joubert, “From Ultrasoft Pseudopotentials to the Projector Augmented-Wave Method,” *Physical Review B,* vol. 59, pp. 1758-1856, 1999.

[57] V.I. Anisimove, J. Zaaen and O.K. Anderson, “Band Theory and Mott Insulators: Hubbard U instead of Stoner I,” *Physical Review B,* vol. 44, pp. 943-1050, 1991.

[58] J. Zhang and R.J. Reeder, “Comparative Compressibilities of Calcite-Structure Carbonates: Deviations from Empirical Relations,” *The American Mineralogist,* vol. 84, p. 861–870, 1999.

[59] A. Navrotsky and L. Chai , “Thermochemistry of Carbonate-Pyroxene Equilibria,” *Contributions to Mineralogy and Petrology,* vol. 114, p. 139–147, 1993.

[60] F. Pertlik, “Structures of Hydrothermally Synthesized Cobalt (II) Carbonate and Nickel(II) Carbonate,” *Acta Cryst,* vol. 42, pp. 4-5, 1986.

[61] H.S. Cheng, “Elasic Anisotropy of Metals,” *Metallurgy Industry Press, Beijing,* p. 20, 1996.

[62] H. Mei, Y. Pang, D. Yu and N. Cheng, “Electronic and Mechanical Properties of Trigonal Boron Nitride by First-Principles Calculations.,” *Physica E: Low-Dimensional Systems and Nanostructures,* vol. 101, pp. 16-21, 2018.

[63] R. Hill, “The Elastic Behaviour of a Crystalline Aggregate,” *Proceedings of the Physical Society, Section A,* vol. 65, pp. 349-355, 1952.

[64] A. Reuss and Z. Angew, “Calculation of the Flow Limits of Mixed Crystals on the Basisof the Plasticity of Monocrystals.,” *Zeitschrift fur Angewandte Mathematik und Mechanik,* vol. 9, pp. 49-58, 1929.

[65] W. Voigt, “Lehrbuch der Kristallpysik Taubner,” *Leipzig,* vol. 213, pp. 29-35, 1928.

[66] S.F. Pugh, “Relations Between Elastic Moduli and the Plastic Properties of Polycrystalline Pure Metals.,” *The Philosophical Magazine,* vol. 45, pp. 823-843, 1954.

[67] K. Lau, “Elastic Anisotropy Factors for Orthorombic, Tetragonal and Hexagonal Crystals,” *Physical Review B,* vol. 58, pp. 8981-8984, 1998.

[68] D.H. Chung and W.R. Buessem, “The Elastic Anisotropy of Crystals,” *Journal of Applied Physics,* vol. 38, pp. 2010-2012, 1967.

[69] N.L. Lethole, P.E. Ngope and H.R. Chauke, “First-principles study: Effect of lithium and sodium intercalation in transition metal phosphates, MPO4 (M: Mn, Fe, Co),” *Computational Condensed Matter,* vol. 22, p. e00437, 2020.

[70] D.P. Dandekar, “Elastic Properties of Calcium Carbonate,” *Journal of Applied Physics,* vol. 39, pp. 3694-3699, 1968.

[71] B.K. Bennazzouz, “A Nanoscale Simulation Study of Elastic Properties of Gaspeite,” *Studia Geotechnicia et Mechanica,* vol. 2, pp. 0015-0050, 2014.

[72] R.J. Bosco and B.G. Jeyaprakash, “Lattice Vibrations, Phonons, Specific Heat Capacity, Thermal Conductivit,” *School of Electrical & Electronics Engineering,* vol. 5, pp. 20-24, 2007.

[73] N.W. Ashcroft and N.D. Mermin, “Solid States Physics,” *New York Holt, Rinehart and Winston,* vol. 8, pp. 826-833, 1976.

[74] K. Parlinski and Y. Kawazoe, “Ab Initio Study of Phonons in Hexagonal GaN,” *Physical Review B,* vol. 60, pp. 15511-15628, 1999.

[75] O.E. Alon and L.S. Cederbaum, “Degenerate Perturbation Theory,” *Physical Review B,* vol. 68, pp. 3310-3430, 2003.

[76] W. Yu, C. Jin and A. Kohlmeyer, “First principles calculation of phonon dispersion, thermodynamic properties and B1-to-B2 phase transition of lighter alkali hydrides,” *Journal of Physics: Condensed Matter,* vol. 19, pp. 086209-086224, 2007.

[77] N.L. Lethole and P.E. Ngope, “Structural, thermodynamic, electronic and mechanical properties of spinel and phonon-harvested AMn2O4 (A: Li, Na, Mg) systems: A First-Principles,” *Materials Today Communications,* https://doi.org/10.1016/j.mtcomm.2019.100704.

[78] Q. Wu, B. He, T. Song, J. Gao and S. Shi, “Cluster Expansion Method and its Application in Computational Materials Science,” *Computational Material Science,* vol. 125, pp. 243-254, 2016.

[79] A. van de Walle and G. Ceder, “Automating First-Principles Phase Diagram Calculations,” *Journal of Phase Equilibria,* vol. 23, pp. 348-351, 2002.

[80] J. M. Sanchez, F. Ducastelle and D. Gratias, “Generalized Cluster Description of Multicomponent Systems,” *Physica A: Statistical and Theoretical Physics,* vol. 128, pp. 334-380, 1984.

[81] D. Lerch, O. Wiekhorst, G. L. W. Hart, R. W. Forcade, and S. Muller, “UNCLE: A Code for Constructing Cluster Expansions for Arbitrary Lattices with Minimal User-Input,” *Modelling Simulation for Material Science Engineering.,* vol. 17, pp. 330-390, 2009.

[82] G.L.W. Hart, S.G. Muller and R.W. Forcade, “UNCLE: A code for constructing cluster expansions for arbitrary lattices with minimal user-input,” *Materials Science and Ingineering,* vol. 5, pp. 0965-0393, 2009.

[83] G. L. W. Hart, V. Blum, M. J. Walorski, and A. Zunger, “Evolutionary Approach for Determining First-Principles Hamiltonians,” *Nature Materials,* vol. 4, pp. 391- 394, 2005.

[84] R.N. Rai, U.S. Rai and K.B.R. Varma, “Thermal, miscibility gap and microstructural studies of organic analog of metal–nonmetal system: p-dibromobenzene–succinonitrile,” *Thermochimica,* vol. 387, p. 101–107, 2002.

[85] W. Cai, “NPT and Grand Canonical Ensembles,” *ME346A Introduction to Statistical Mechanics* , vol. 3, pp. 1-12, 2011.

[86] J. F. Nye, “Physical Properties of Crystals,” *Clarendon Press: Oxford University Press,* vol. 36, pp. 506 - 575, 1985.

[87] A. Chakraborty, S. Kunnikuruvan and S. Kumar, “Layered Cathode Materials for Lithium-ion Batteries,” *Chemistry of Materials,* vol. 32, pp. 915-952, 2020.

[88] W.A. Curtin and R.E. Miller, “Modelling and Simulation in Material Science and Engineering,” *Computational Materials,* vol. 11, pp. 110-133, 2003.